Study of fusion evaporation channels in the $^{18}O + ^{18}O$ reaction at 65 MeV

by

Esra Ahmed Mohammed Adam Khaleel

Thesis presented in partial fulfilment
of the requirements for the degree of
Master of Science
at Stellenbosch University

Supervisor: Dr Paul Papka
Co-Supervisor: Dr Simon Mullins

December 2011

Declaration

By submitting this thesis electronically, I declare that the entirety of the work contained therein is my own, original work, that I am the sole author thereof (save to the extent explicitly otherwise stated), that reproduction and publication thereof by Stellenbosch University will not infringe any third party rights and that I have not previously in its entirety or in part submitted it for obtaining any qualification.

Date:----------"

Abstract

The fusion evaporation reaction is mainly used to populate high spin states in atomic nuclei. Using stable beams, a large number of β^+ unstable nuclei were studied i.e. those nuclei on the neutron deficient side of the valley of stability. A plethora of experimental data is available in a wide range of mass $A \sim 20$ to $A \sim 250$ and was used to test the statistical model codes such as PACE, CASCADE, GEMINI.

With the advent of radioactive beams, a new landscape will be available to provide further tests to the models. However, a study of fusion evaporation reactions will only be possible with sufficient beam intensities. In this thesis β^- unstable nuclei were populated with one of the few reactions where nuclei approaching the neutron rich region can be populated with stable beams. The aim of this thesis is to study the fusion evaporation channels of the ^{18}O + ^{18}O reaction at a beam energy of $E_{lab} = 65$ MeV in order to populate the ^{36}S compound nucleus. Due to the relatively low Coulomb barrier the evaporation of charged particles is a relatively strong channel.

The DIAMANT light charged particle detector was set in coincidence with the AFRODITE γ-ray spectrometer to trigger between light charged particles and γ-rays. ROOT package software and SimSort code were used to perform the data analysis as well as the simulation. The coincident data allows the evaporation channels involving *p, d, t* and α particles to be identified due to excellent particle identification with the CsI charged particle detectors while the A, Z of the residual nuclei are identified with the gamma transitions measured with germanium detectors.

In this thesis, the cross sections of the residual nuclei were calculated with the statistical model code CACARIZO, a Monte Carlo version of CASCADE based on the Hauser-Feshbach formalism. Experimental and theoretical results and charged particle energy spectra are compared.

Opsomming

Die samesmeltings-verdampingsreaksie is hoofsaaklik gebruik om die hoë spin toestande in atoom kerne te vul. Deur stabiele bundels te gebruik word 'n groot aantal β^+ onstabiele kerne bestudeer d.w.s. daardie kerne op die neutron arme kant van die vallei van stabiliteit. Baie van die eksperimentele data is beskikbaar in 'n wye gebied van massas $A \sim 20$ tot $A \sim 250$ en word gebruik om die statistiese model kodes soos PACE, CASCADE, en GEMINI te toets.

Met die beskikbaarheid van radioaktiewe bundels sal nuwe landskappe beskikbaar gestel word wat verdere toetse van hierdie modele moontlik maak. Die studie van smeltingsverdampings reaksies sal egter net moontlik sal wees met genoegsame bundel intensiteite. In hierdie tesis word β^- onstabiele kerne gevul met een van 'n paar reaksies waardeur die kerne bereik kan word vanaf die neutron ryke gebied en bevolk word met behulp van stabiele bundels. Die doel van hierdie tesis is om 'n studie te maak van die smeltingsreaksie kanaal van die ^{18}O + ^{18}O reaksie by 'n bundel energie van $E_{lab} = 65$ MeV om die ^{36}S saamgestelde kern te bevolk. Weens die relatiewe lae Coulomb wal is die verdamping van gelaaide deeltjies 'n relatiewe sterk kanaal.

Die DIAMANT lighe deeltjie detektor was in ko-insidensie gesit met die AFRODITE γ-stralings spektrometer om tussen ligte gelaaide deeltjies en γ-strale af te vuur. Die ROOT sagteware pakket en SimSort kodes was gebruik om die data-analise asook die simulasies te doen. Die ko-insidensie data laat toe dat die verdampingskanaal waarby p, d, t en α deeltjies betrokke is te identifiseer weens uitstekende deeltjie identifikasie met die CsI gelaaide deeltjie detektor terwyl die A, Z van die residuële kerne met γ oorgange wat gemeet is met germanium detektor geidentifiseer word.

In hierdie tesis word die kansvlakke van die residuële deeltjie bereken met die statistiese model kode CACARIZO, wat 'n Monte Carlo weergawe is van CASCADE wat gebaseer

is op die Hauser-Feshbach formalisme. Eksperimentele en teoretiese resultate en gelaaide deeltjie energie spektra word vergelyk.

Acknowledgments

Foremost, I would like to express my sincere gratitude to my supervisors Dr. Paul Papka and Dr. Simon Mullins for the continuous support of my MSc study and research, for their patience, motivation, enthusiasm, and immense knowledge. Their guidance helped me in all the time of research and the writing of this thesis. I could not have imagined having better supervisors for my MSc study.

My sincere thanks also goes to Dr. Shaun Wyngaardt, the nuclear physics group leader for his valuable help. Also, I have to express my gratitude to the African Institute for Mathematical Sciences (AIMS) and the National Institute for Theoretical Physics at the University of Stellenbosch for the Scholarships and without them I wouldn't have this chance to study.

Last but not the least, I would like to thank my family: my parents Ahmed Mohammed Adam khaleel and Samira Mohammed Momen Nasor, for guiding and supporting me, and for their love throughout my life; My dearest brother Mohammed Elfatih and my lovely sisters Asmaa, Alaa and Elkhansaa. I am really grateful to all of you for the love and support.

But above all my sincere gratitude to Almighty Allah for everything.

Contents

List of Figures

List of Tables

Chapter 1

Introduction

The fusion evaporation reaction is a mechanism which favorably populates high spin states and are expected to favor the emission of light particles more effective than nucleons in removing angular momentum. This effect contributes to further complicate the decay cascade. The population of high spin states may induced angular momentum driven from dynamical deformations of the hot nucleus [7]. Fusion evaporation mechanism has been utilized to study nuclei in the neutron deficient region. Large amount of experimental data is available to test the statistical model codes such as PACE [8], GEMINI [9] and CASCADE [10]. Fusion evaporation reactions populate compound nuclei as an intermediate state as proposed by Bohr [11] for the first time. Compound nucleus formation can lead to the production of very neutron deficient nuclei by evaporation of neutrons. This work focuses on the study of fusion evaporation channels in the ^{18}O + ^{18}O reaction where specific decays lead to the population of P, Si neutron rich nuclei from the ^{36}S compound nucleus. In this work, coupling between a γ-ray spectrometer, AFRODITE, and a light charged particle detector, DIAMANT, was employed in order to isolate specific decay channels. Statistical theory appears to fit the data of heavy-ion-induced reactions when the basic formalism of the model is applied at each decay step and summed over all the decay products. The basic formalism includes the relevant structure information available for nuclei near the valley of stability in the form of the Optical Model (OM) transmission coefficients and the level densities based on light-particle-induced reaction studies [7]. Theoretical calculations using the statistical model code CACARIZO [12], the Monte Carlo version of CASCADE, performed and compared to some aspects of the experimental data collected at the iThemba

LABS facility of Cape Town. In this thesis we report on a very selective and origin results of deuteron-to-proton and triton-to-proton ratios of very selective transitions of ^{32}P and ^{30}Si as well as the calculated particle energy spectra compared to the experimental data. The aim of this investigation is to test the statistical model codes in nuclear region that has not been tested before and check the reliability of such codes for future use.

1.1 Thesis Layout

In this work, evaporation of light charged particles is presented as a result of the study of the fusion evaporation channels in the ^{18}O + ^{18}O reaction at 65 MeV. In chapter 2, an introduction to the compound nucleus theory and its formation is discussed. The fusion evaporation mechanism to populate compound nuclei with high excitation is discussed with details of the cascade emission of the light charged particles beside the theoretical statistical model of nuclear evaporation based on the Hauser-Feshbach formalism. The computer code CACARIZO, the Monte Carlo version of CASCADE, is discussed with emphasis on the input parameters. The performance of the experiment, the experimental set up and arrangement of the AFRODITE γ-ray spectrometer and the DIAMANT charged particle detectors are discussed in chapter 3. In chapter 4, the experiment details and the data analysis procedures, including the calibration of both the AFRODITE and DIAMANT detectors and particle identification of the detected light charged particles, are discussed. The total projections of γ-rays gated on light charged particles are also presented. Chapter 5 is devoted to the statistical model calculations and the step-by-step simulation of the ^{18}O + ^{18}O reaction. The relative cross sections of the residual nuclei are also calculated. The results of this research work and their interpretations are discussed in chapter 6. The results include the deuteron to proton and triton to proton ratio of the main residual channels. The calculated energy spectra of the proton, deuteron, triton and α-particles are compared to the experimental distributions. Finally, the conclusion and the future outlook are discussed in chapter 7.

Chapter 2

Theoretical Calculations

2.1 Introduction to Compound Nucleus Theory

In fusion reaction, formation of a compound nucleus is dominant mainly at low incident energies. There are several studies that have been made in the past to describe the properties of the compound nucleus. The first model of a compound nucleus reaction was the evaporation theory by Bethe and Weisskopf in 1937 [13]. Later studies were made by Weisskopf and Ewing in 1940, who wrote the expression for the cross-sections of compound nucleus reaction to continuum states. In the early 1950's, Hauser and Feshbach developed a formalism to calculate the cross-sections of compound nucleus formation to discrete final states by introducing quantum mechanics [13]. In 1958 and 1968, there were studies made by Thomas and Vogt respectively. The recent developments were made in the late 1970s by Mahaux and Weidenmuller. In 1980, Feshbach *et al.* included the multi-step processes in the theory of compound nucleus formation [13]. The studies by Feshbach *et al.* is known as EHFM the Extended Theory of the Hauser-Feshbach Model [14]. This chapter will discuss the CACARIZO code from 1977 based on the Hauser-Feshbach formalism which gives the numerical calculations of the cross-sections by Hauser-Feshbach.

2.2 The Optical Model

The Optical Model successfully describes the scattering processes within the interaction between two colliding nuclei in heavy-ion reactions. The Optical Model simplifies the interaction between two nuclei by considering this interaction as a two-body complex potential which includes the scattering and the absorption of the incident particles. The simplest form of the Optical Model can be described by Eq. 2.1 [15],

$$U(r) = V(r) + iW(r) \tag{2.1}$$

where the absorption of the incident particle into the target nucleus to form a compound nucleus is represented by the imaginary part of the potential $W(r)$, and the elastic scattering is represented by the real part of the potential $V(r)$ [16, 17].

2.3 Compound Nucleus Formation

In many types of nuclear reactions, the projectile particles can possibly be absorbed by the target nucleus to form the so-called compound nucleus. This type of reaction is likely to occur at energies above the Coulomb barrier which leads to a high excitation energy and large angular momentum. Within the range of 10^{-20} s, the compound nucleus cools down by emitting proton, neutron and α particles or other light charged particles. Therefore, the residual nucleus is still in an excited state and de-excites by emitting γ-rays within a typical time of 10^{-15} s until it reaches its ground states. This entire process takes place within a characteristic time of about 10^{-12} second. Nuclear reactions where a formation of a compound nucleus are found to be of particular interest. It gives good results of forming compound nuclei with high excitation energy in order to study high spin states. In high spin states, the formation of a compound nucleus depends on the limitation of the maximum angular momentum that can be carried by the compound nucleus. The impact parameter plays an important role in the calculations of the compound nucleus cross sections in heavy ion reactions [18].

The continuous spectra of the particles evaporated from the residual nuclei can be treated and analyzed by the semi-classical statistical model. The statistical model of a compound

nucleus is based on the Hauser-Feshbach formalism (1952) [19, 18] and it is used to calculate the differential cross sections for each of the cascades from their spins, parities and the appropriate transmission coefficients.

2.4 Fusion Evaporation Reaction

A compound nucleus can be formed by bombarding a beam particle on a target nucleus. If the energy of the incident particle is enough to overcome the Coulomb barrier, given by Eq. 2.2, then the formation of a compound nucleus with an excitation energy defined by the incident energy and the Q value will occur.

$$V_{CB} = \frac{1}{4\pi\epsilon_0}\frac{z_p z_t e^2}{R} \tag{2.2}$$

where z_p and z_t are the atomic numbers of the projectile and target nuclei, respectively. R is the distance between the two charge centers when the nuclei are in contact, e is the charge of an electron and ϵ_0 is the permittivity of free space.

De-excitation of the compound nuclei proceeds by emission of a number of particles such as neutrons, protons, deuterons, tritons and α particles. When the excitation energy of the residual is below the particles binding energy, these residual nuclei de-excite by emission of a cascade of γ-rays until the residual nuclei reach their ground states [20]. A typical excitation energy removed by particles is in the order of 10 MeV per particle emitted [21] and energy of the emitted γ-rays is in the order of under a few MeV. An illustrative example of a fusion evaporation reaction is illustrated in Fig. 2.1.

2.5 Statistical Theory of Nuclear Reactions and Nuclear Evaporation

In statistical nuclear reaction theory, the Optical Model is used to calculate the cross section of nuclear reactions. There are two main types of nuclear reactions classified according to their typical times. The first type is the fast process where the duration of reaction is comparable to the time needed by the incident projectile to pass through the target nucleus

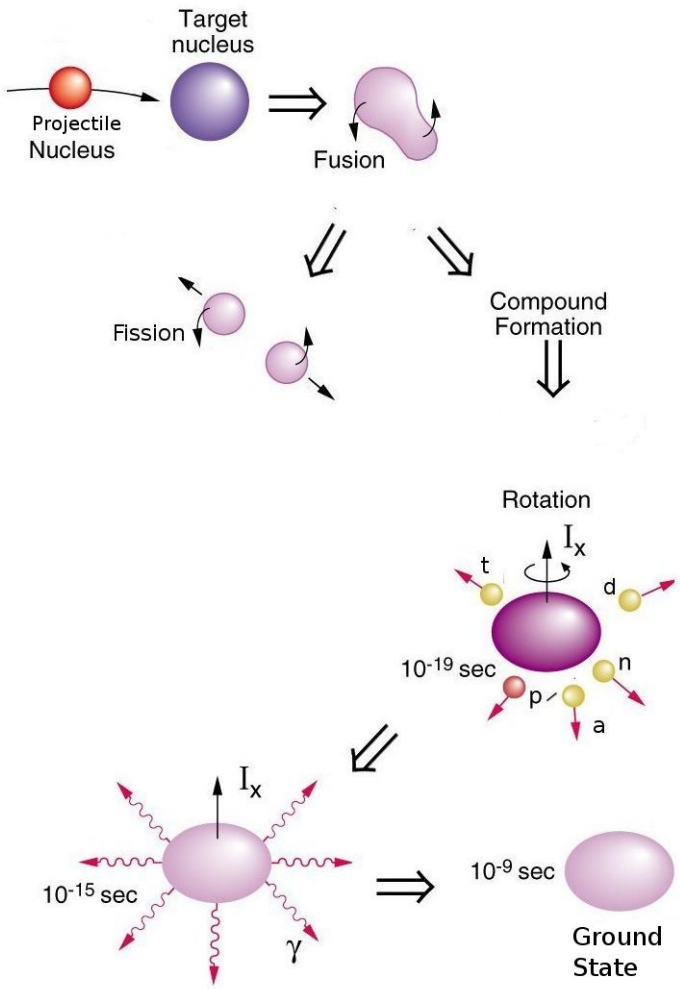

FIG. 2.1. Schematic diagram of the fusion evaporation mechanism.

without interacting. The second type is the slow process. Therefore, the statistical model of a nuclear reaction (or compound nucleus formation) is considered as a slow nuclear reaction. In the statistical model, a compound nucleus is formed with high excitation energy after the beam projectile has been absorbed by the target nucleus. Moreover, the incident energy is shared between the nucleons inside the compound nucleus. This indicates that the compound nucleus decays without recognizing the entrance channel effects. In addition to the fundamental equations of the statistical nuclear model approach, the parameters characterizing the Fusion Evaporation reaction are discussed in the following sections as well as the Hauser-Feshbach formalism and its parameterizations.

2.6 Fundamental Equations of the Statistical Model

2.6.1 Reaction Channel Definition

A general form of a nuclear reaction to be treated by the statistical nuclear model is described in Eq. 2.3,

$$a + A \rightarrow CN^* \rightarrow B + b \tag{2.3}$$

where a is the beam projectile, A is the target nucleus, CN^* is the intermediate excited compound nucleus, b is the ejectile and B is the residual nucleus. In any nuclear reaction, some observable quantities must be conserved after the reaction. These quantities are written as follows,

- Total energy conservation: $E_a + E_A = E_B + E_b + Q$,
- Total momentum conservation: $\vec{p}_a + \vec{p}_A = \vec{p}_B + \vec{p}_b$,
- Total angular momentum conservation: $\vec{l}_a + \vec{s}_a + \vec{I}_A = \vec{J}_C = \vec{l}_b + \vec{s}_b + \vec{I}_B$,
- Total parity conservation: $(-1)^{l_a}\pi_a\pi_A = \pi_C = (-1)^{l_b}\pi_b\pi_B$

2.6.2 Hauser-Feshbach Formalism

The statistical model codes, such as CASCADE [10], PACE [8] and LILITA [22, 23], calculate the energy distribution of the evaporation residues after emission of light charged particles from a compound nucleus based on the Hauser-Feshbach formalism. The basic idea of the Hauser-Feshbach formalism is based on the Bohr independence hypothesis that assumes any nuclear reaction forms a compound nucleus first as an intermediate state, then it decays to the final states by emission of light particles. In this section, a brief discussion of the numerical description of the Hauser-Feshbach theory of the cross section is considered. The Hauser-Feshbach formalism treats the cross-section ($\sigma_J^{(c)}$) of the formation of a compound nucleus and its statistical chain decay to channel c populated with a total angular momentum J and at excitation energy (E_x) given by Eq. 2.4 [14]:

$$\sigma_J^{(c)} = R_J^{(c)}\sigma_J(E_x) \tag{2.4}$$

where,

- $\sigma_J(E_x)$ is the cross-section of the populated compound nucleus.
- $R_J^{(c)}$ is the decay ratio and is determined by the ratio of the partial width $\Gamma_J^{(c)}$ to the total width Γ_J and is given by Eq. 2.5.

$$R_J^{(c)} = \frac{\Gamma_J^{(c)}}{\Gamma_J} \tag{2.5}$$

where the total width Γ_J is given by the sum of all the partial widths of all the possible decaying channels c and can be written as in Eq. 2.6 [14]:

$$\Gamma_J = \sum_c \Gamma_J^{(c)}. \tag{2.6}$$

The decay channel c includes neutron, proton, α-particles and emission of γ-rays. In this study, the decay channel c includes deuteron and triton beside neutron, proton and α-particles. The partial width $\Gamma_J^{(c)}$ is related to a phase space integration and is given by Eq. 2.7 [14]:

$$\rho_J(E_x)\Gamma_J^{(c)} = \frac{1}{2\pi} P_J^{(c)}. \tag{2.7}$$

$\rho_J(E_x)$ is the level density of the compound state. This level density is used to estimate the mean lifetime of a compound state. The mean lifetime τ_J of a compound nucleus is generally estimated by using the total width Γ_J following Eq. 2.8

$$\tau_J = \frac{\hbar}{\Gamma_J} \tag{2.8}$$

The phase space $P_J^{(c)}$ of a channel c is evaluated by the phase space integration described in Eq. 2.9

$$P_J^{(c)} = g_c \sum_{(L,I)J} \int\int \rho_I(\epsilon) T_L(E) \delta(\epsilon + E + Q - E_x) d\epsilon dE. \tag{2.9}$$

where:

- g_c is the spin multiplicity of the evaporated particle.
- $\rho_I(\epsilon)$ is the level density of the residual nucleus with an angular momentum I and excitation energy ϵ.

- $T_L(E)$ are the transmission coefficients for the evaporated light particles as a function of the excitation energy E.
- The $(L, I)J$ shown in the summation represents the coupling condition of the angular momentum, where the energy conservation condition is maintained by $\delta(\epsilon + E + Q - E_x)$.

At the end of the cascade, the excited states of the daughter nucleus are low enough so that the phase space integrations of the light particle decay is considered as discrete levels of the daughter nucleus near its ground state. Consequently, the phase space integration $P_J^{(c)}$ becomes a summation of all known discrete levels i of the daughter nucleus instead of the energy integration and follows Eq. 2.10,

$$P_J^{(c)} = g_c \sum_i \sum_{(L,I_i)J} \int T_L(E)\delta(\epsilon_i + E + Q - E_x)dE. \tag{2.10}$$

ϵ_i and I_i are the energy and spin of the known i^{th} discrete levels of the daughter nucleus respectively. The observable Q in Eq. 2.9 and Eq. 2.10 is the separation energy of a light particle to be emitted from a nucleus and is defined in Eq. 2.11

$$Q = B_{GS}(N_{CN}, Z_{CN}) - B_{GS}(N_L, Z_L) - B_{GS}(N_H, Z_H) \tag{2.11}$$

$B_{GS}(N_{CN}, Z_{CN})$, $B_{GS}(N_L, Z_L)$ and $B_{GS}(N_H, Z_H)$ are the binding energies of the compound nucleus, evaporated light particle and the residual nucleus respectively. For the level density calculation, the classical Bohr and Mottelson equation [11], which is derived from the Fermi gas model, is used

$$\rho_I(\epsilon) = \frac{1}{12}(\frac{a\hbar^2}{2\mathcal{J}})^{3/2}(2I+1)a\frac{e^{2\sqrt{X}}}{X^2} \tag{2.12}$$

where

$$X = a(\epsilon - \frac{\hbar^2}{2\mathcal{J}}I(I+1) - \Delta_{pair}). \tag{2.13}$$

$\mathcal{J}$ is the moment of inertia of the daughter nucleus, $\Delta_{pair} = 12/\sqrt{A}$ is the pairing energy, while a is the level density parameter and is rather an arbitrary parameter but normally is set to be $a = A/8$ [24, 25, 26].

2.7 The Computer Code CACARIZO

CACARIZO [12] is the Monte Carlo version of the computer code CASCADE and is used to calculate the cooling of a compound nucleus by the emission of light particles. In this computer code a step by step calculation of the emission of light particles is considered by including the spin coupling between the light particles (LP) and the compound nucleus.

In CACARIZO, the Hauser-Feshbach formalism, as discussed in section. 2.6.2, is used to calculate all the possible evaporation chains of neutrons, protons, α particles and followed by the emission of γ-rays until the residual nucleus reaches its ground state. The probability of a compound nucleus with specific excitation energy (E_x), angular momentum (J_l) and parity π_l to evaporate a light particle with an orbital momentum (l), spin (s) and a kinetic energy (E_l) in an energy interval dE_l is given by Eq. 2.14 [12].

$$P_x dE_l = \frac{1}{\hbar}\Gamma(E_l) = \frac{\rho_2(E_{x2}, J_2, \pi_2)}{2\pi\hbar\rho_1(E_{x1}, J_1, \pi_1)} \sum_{S=|J_2-s|}^{J_2+s} \sum_{l=|J_1-S|}^{J_1+S} T_l(E_l) dE_l \tag{2.14}$$

Where E_{x2}, J_2 and π_2 are the excitation energy, angular momentum and parity of the daughter nucleus respectively. ρ_1 and ρ_2 are the level densities of the parent and daughter nuclei respectively. $T_l(E_l)$ are the transmission coefficients of the evaporated particle.

2.7.1 The input parameters of the CACARIZO

In the statistical model equations, two types of parameters are considered, the transmission coefficients and the level density. In the following sections, particle transmission coefficients is considered and will be discussed briefly with the parametrization of the Yrast line and the critical angular momentum.

Transmission coefficients

The function $T_L(E)$, mentioned earlier in Eq. 2.9 and Eq. 2.10, is known as the transmission coefficients. It describes the probability of emission of a light particle as a function of its kinetic energy and the angular momentum of the compound nucleus. The simplified

expression of the transmission coefficients is given by Eq. 2.15 [14]:

$$T_L(E) = \frac{1}{1 + \exp[(V(L) - E)/\Delta_s]} \tag{2.15}$$

where Δ_s is the diffuseness parameter, with given the value of 0.5 MeV, and $V(L)$ is the parametrization of the barrier height at the scission point consisting of the Coulomb and the centrifugal potential and is taken into account on its simplest form as

$$V(L) = V_{coul} + \frac{\hbar^2}{2\mu_f R_s^2} L(L+1). \tag{2.16}$$

where V_{coul} is the Coulomb barrier given by equation 2.2, μ_f is the reduced mass of the decaying complex fragments and the scission point Rs is determined by using the radius $R_L = r_0 A_L^{1/3}$ and $R_H = r_0 A_H^{1/3}$ of the light and heavy fragments respectively of mass number A_L and A_H including the diffuseness effects with a separation distance d given by expression 2.17.

$$R_s = R_L + R_H + d \tag{2.17}$$

Parametrization of the Yrast line

The Yrast state is the minimum energy state of a nucleus when it is least excited for a given angular momentum. The rotational energy of a nucleus is represented by the Yrast line [27] described by Eq. 2.18,

$$E_{rot} = \frac{\hbar^2}{2\mathcal{J}} J(J+1) \tag{2.18}$$

where $\mathcal{J}$ is the moment of inertia of a rigid body [28]. In the CACARIZO code, the calculations take into account the deformability δ of a liquid drop. Therefore, the moment of inertia of a deformable liquid drop as considered by the CACARIZO code is described by Eq. 2.19

$$\mathcal{J}(J) = \mathcal{J}_{sphere}(1 + \delta_1 J^2 + \delta_2 J^4) \tag{2.19}$$

where $\mathcal{J}_{sphere}$ is the moment of inertia of a spherical nucleus given by $\mathcal{J}_{sphere} = \frac{2}{5} r_\circ^2 A^{5/3}$, with A the mass number of the nucleus [29], and $\delta_{1,2}$ are the deformability parameters. The formation of a compound nucleus and its decay by the evaporation of light charged particles is described in Fig. 2.2 as well as the γ decay of the residual nucleus and the Yrast line as a function of the angular momentum.

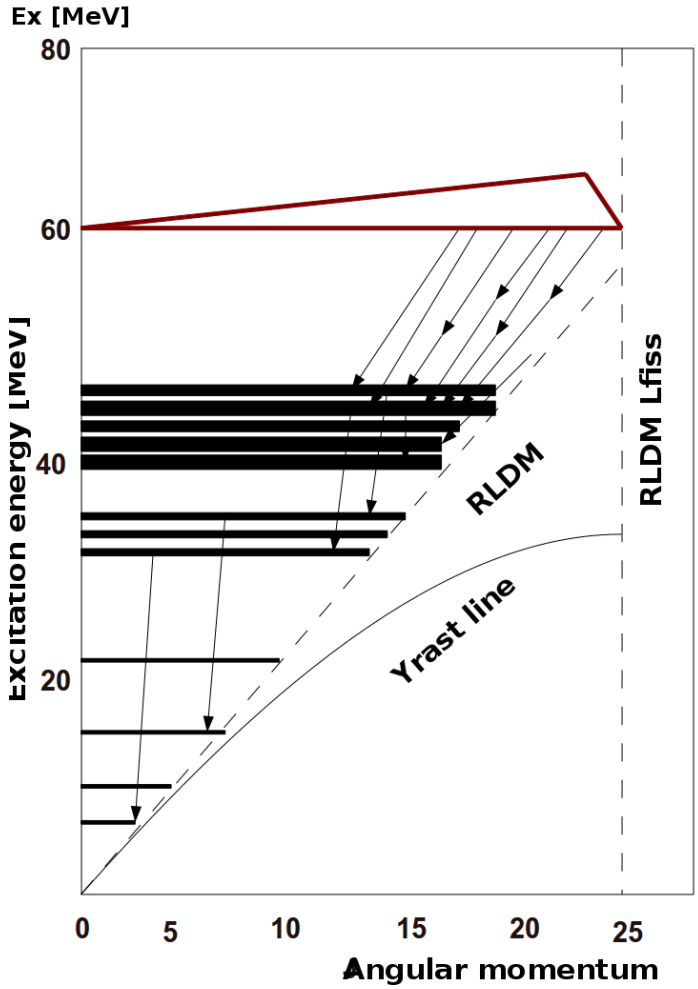

FIG. 2.2. Population of ^{36}S from the ^{18}O + ^{18}O reaction with excitation energy Ex = 61.6 MeV and total angular momentum J = 25$\hbar$.

Critical angular momentum

The fusion cross section is limited by a critical angular momentum for a compound nucleus. Therefore, at angular momentum higher than the critical angular momentum, the fission process will dominate and the compound nucleus formation can not exist at these energies. The complete fusion cross section is determined by the formula in Eq. 2.20 [30].

$$\sigma_{fus} = \sum_{J=0}^{\infty} \sigma_{fus}(J) = \pi\lambda^2 \sum_{J=0}^{\infty} (2J+1) T_{(J)}^{(fus)} \tag{2.20}$$

where λ and J are the reduced wavelength and the total angular momentum of the entrance channel of the reaction. For simplicity, the transmission coefficients $T_{(J)}^{(fus)}$ are represented by the Fermi distribution as described in Eq. 2.21 [14].

$$T_{(J)}^{(fus)} = \frac{1}{1 + exp[(J - J_{cr})/\delta_J]} \tag{2.21}$$

J_{cr} is the critical angular momentum and is used to reproduce the fusion cross section of the complete fusion σ_{fus} and simply Eq. 2.20 can be rewritten as follows [31].

$$\sigma_{fus} = \pi\lambda^2 \sum_{J=0}^{J_{cr}} (2J + 1) = \pi\lambda^2 (2J_{cr} + 1)^2 \tag{2.22}$$

Fig. 2.3 is describing the complete fusion cross section for the ^{18}O + ^{18}O reaction at E_{lab} = 65 MeV as a function of the energy which is calculated using a Monte Carlo simulation code [11].

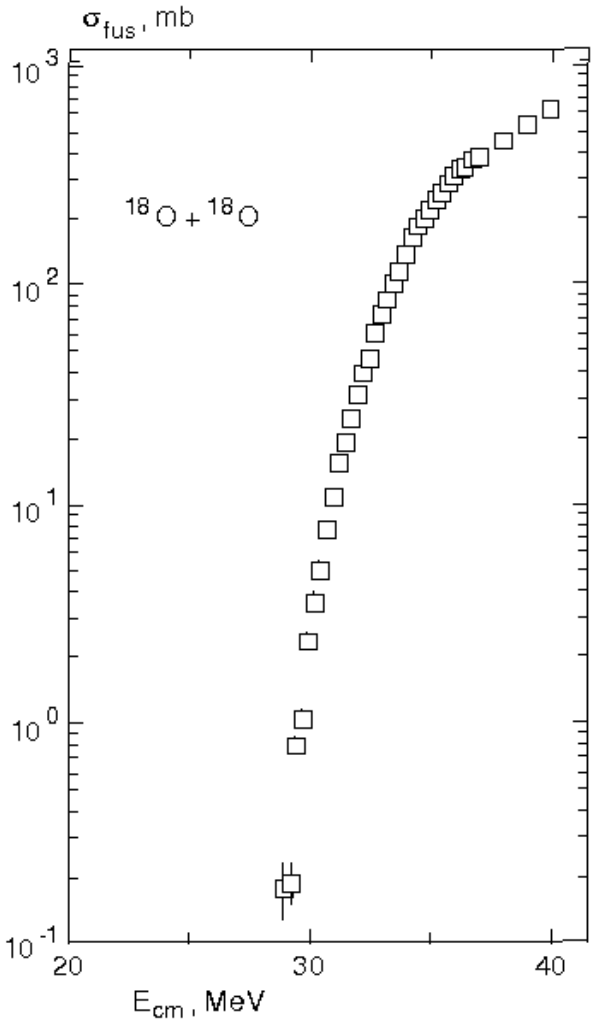

FIG. 2.3. The complete fusion cross section of the ^{18}O + ^{18}O system as a function of energy [1, 2].

Chapter 3

Experimental Methods

In this chapter, γ-rays and their interaction with matters are discussed in detail with charged particle detection. More emphasis on the experimental demonstration and data acquisition system are discussed.

3.1 Interaction of γ-rays with Matter

When γ-rays are emitted from an excited nucleus, a set of detectors can be utilized to measure the energy of these high energy photons. This detection of γ-rays occur after an interaction between the incident photon and the effective material of the detector. There are three possible mechanisms of the interaction of γ-rays with matter which are the Photoelectric Effect, Pair Production and Compton Scattering and will be discussed in the following sections.

3.1.1 Photoelectric Effect

When an incident γ-ray with energy (E_γ) interacts with the detector material, it gives all of its energy to an atom. Therefore, the atom is excited and subsequently a bound electron will be released with a kinetic energy (E_e). This process is known as the photoelectric effect and is illustrated in Fig. 3.1.

The kinetic energy of the emitted electron is equivalent to the binding energy (E_b) of the

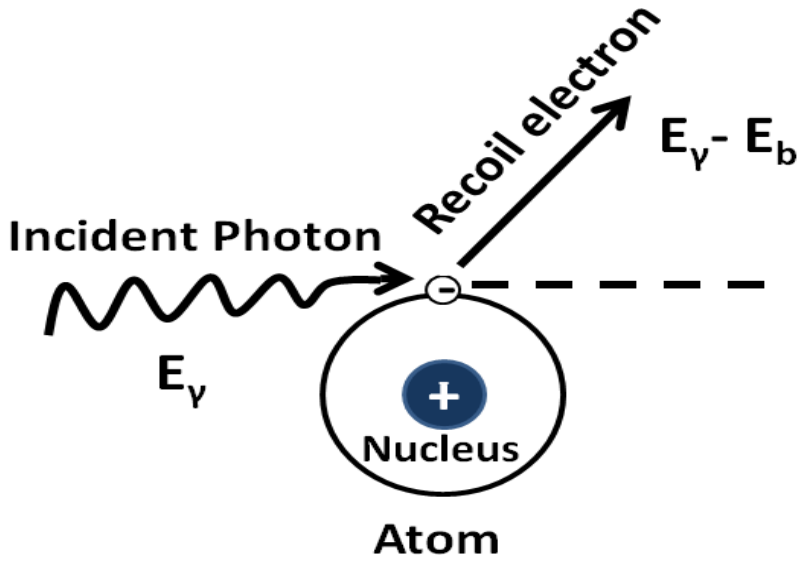

FIG. 3.1. Schematic diagram illustrating the Photoelectric Effect process.

electron subtracted from the incident γ-ray energy which is given by Eq. 3.1 [4].

$$E_e = E_\gamma - E_b \tag{3.1}$$

The photoelectric effect can not occur between the photon and a free electron because the energy and momentum will not be conserved. Therefore, the conservation of energy and momentum in the photoelectric effect is valid by including the momentum of the parent atom as well because part of the momentum will be transfered to the parent atom, however, $m_e << m_{atom}$ and most of the energy is carried by the electron. The photoelectric effect is dominant for γ-ray energies below 200 keV [32].

3.1.2 Compton Scattering

Compton scattering is a process when an incident γ-ray with energy E_γ scatters of an atomic electron where part of the γ-ray energy is transfered to the scattered electron and the remaining energy E'_γ is carried away by the scattered photon. This process is illustrated in Fig. 3.2.

The kinematic relation between the incident and the scattered photon energy of this process

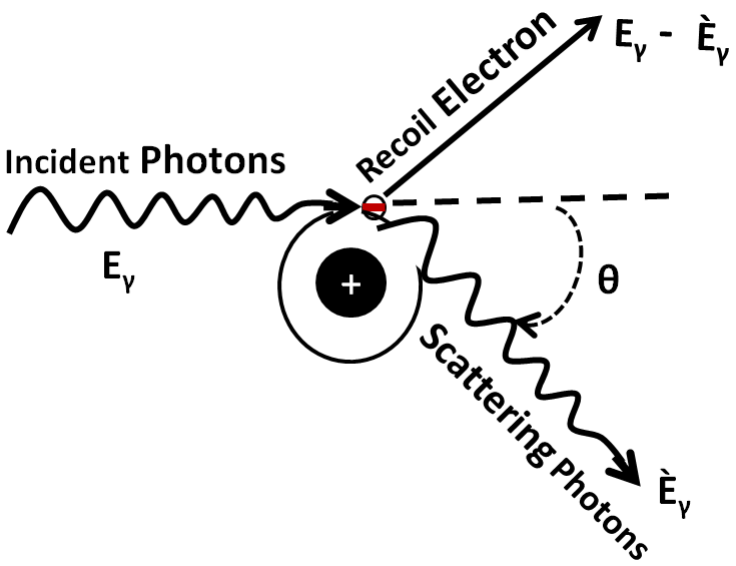

FIG. 3.2. Schematic diagram showing the mechanism of the Compton scattering process.

is given by Eq. 3.2,

$$E'_\gamma = \frac{E_\gamma}{1 + \frac{E_\gamma}{m_e c^2}(1 - cos\theta)} \tag{3.2}$$

Where:

- $m_e c^2$ is the rest mass energy of the electron equal to 511 keV.
- θ is the scattering angle of the photon, where the maximum energy transfer happens when $\theta = 180^o$.

The mechanism of Compton scattering is dominant in the region between 200 keV to 1 MeV [33, 32]. In this study, the Compton scattering occurs in the measurement of the coincidence γ-rays by the Clover detectors in the AFRODITE spectrometer, where Compton scattering increases the background of the measurements. Therefore, the BGO shield was used to eliminate the background.

3.1.3 Pair Production

In order to produce an electron-positron pair in the interaction of a γ-ray with matter, the energy of the incident photon must be sufficient in order to remove an electron-positron

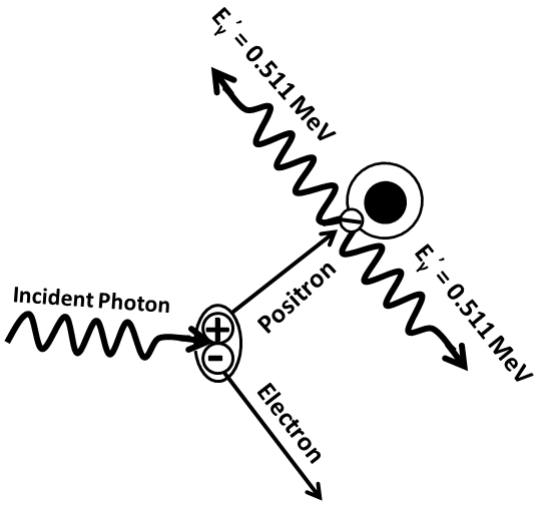

FIG. 3.3. Schematic diagram illustrating the pair production process.

pair from an atom. In other words, the incident energy must be greater than the total rest mass energy of the electron-positron pair which is 1.022 MeV [32]. The excess energy appears as kinetic energy of the electron-positron pair.

As soon as the electron-positron pair is produced, the positron firstly slows down by interacting with the surrounding environment and after slowing down it picks an electron from the surrounding medium to form a positronium bound system like the hydrogen system. Therefore, the positronium annihilates into two or three gamma-rays depending on the spin alignment of the electron and the positron [34, 35, 36, 37].This annihilation of γ-rays may escape from the detector or they might both be absorbed. If both annihilated γ-rays are absorbed in the detector, the interaction gives the full energy peak of the measured spectrum. If one of the annihilated γ-rays escapes from the detector, the interaction will contribute to the single escape peak with 0.511 MeV below the full energy peak and when both γ-rays escape, the interaction contributes to the double-escape peak with 1.022 MeV below the full energy peak [38].

3.2 Doppler Shift and Doppler Broadening

In this experiment, both thick and thin targets were used. In the case of thin target, the residual nuclei recoil from the target so that the γ-rays emitted from these recoil residuals were intend to be broad peaks because of the Doppler shift. Hence a Doppler correction must be made to the emitted γ-rays which is given by Eq. 3.3 [39, 33],

$$E_{\gamma}^{'} = E_{\gamma}(1 + \beta cos\theta) \tag{3.3}$$

Where:

$E_{\gamma}^{'}$ is the Doppler shifted γ-ray energy.

E_{γ} is the unshifted γ-ray energy.

θ is the angle between the direction of the γ-rays and the initial direction of motion of the emitter.

$\beta = v/c$, where v is the velocity of the recoil nucleus at decay and c is the speed of light. In this work, the value of β is calculated to be 0.044% of the speed of light c.

3.3 Experimental Set Up

For the investigation of the structure of light neutron rich nuclei populated in the ^{18}O + ^{18}O fusion evaporation reaction, the AFRODITE γ-spectrometer is used to measure the energy of the γ-rays in $\gamma - \gamma$ coincident events. The DIAMANT detector was operated in order to trigger between evaporation channels containing charged particle. This chapter will discuss in details the AFRODITE array, the DIAMANT detector and the experimental setup used in this experiment.

3.3.1 AFRODITE Array

AFRODITE is an acronym of the AFRican Omni-purpose Detector for Innovative Techniques and Experiments. The AFRODITE γ-spectrometer was assembled at iThemba

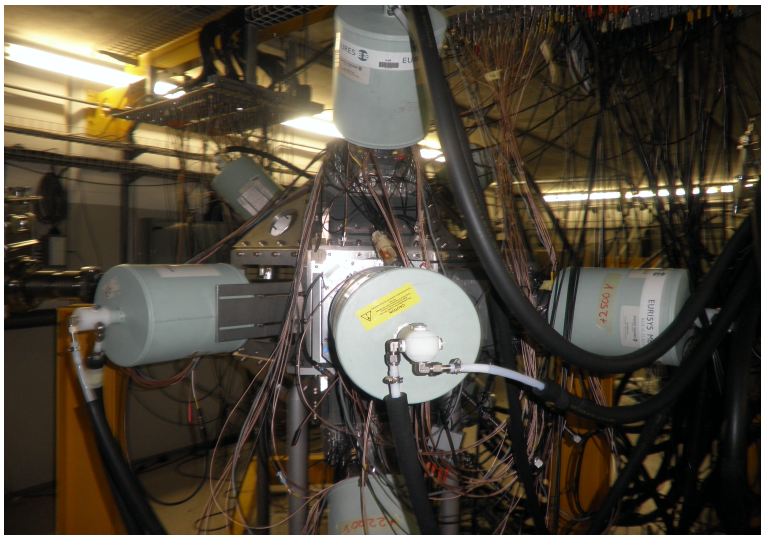

FIG. 3.4. The AFRODITE γ-detector

Laboratory for Accelerator Based Sciences (LABS) in Cape Town-South Africa and was lunched in 1998 to detect both high and low energy photons in the order of few keV to 20 MeV. The AFRODITE is mounted in a frame with a rhombicuboctahedron shape with sixteen detector positions. The AFRODITE is a medium sized array consisting of a combination of large volume escape suppressed High Purity Germanium (HPGe) detectors, the Clover detectors (see Sec. 3.3.2), and Low Energy Photon Spectrometer (LEPS) detectors as depicted in Fig. 3.4. The AFRODITE γ-spectrometer has seventeen detectors, nine Clover detectors and eight LEPS for detecting photons with incident energies between 30 keV and 2 MeV. These detectors were arranged in three different rings and placed at 45° with eight position detectors, 90° with four positions and 135° degrees with four positions with respect to the beam direction. The target chamber is positioned at the center of the AFRODITE array as depicted in Fig. 3.7.

This combination gives a unique feature to AFRODITE to be able to detect both high and low energy photons with relatively high efficiency. The measured full energy peak efficiency of the AFRODITE array is 1.5% at 1.3 MeV and $9(2)\times10^{-4}$ at 15 MeV [40].

3.3.2 Clover detector

Each Clover detector of the AFRODITE is positioned inside a symmetric Bismuth Germanate ($Bi_4Ge_3O_2$) suppression shield known as BGO and shown in Fig. 3.6. The Clover detectors consist of four separate co-axial N type High Purity Germanium (HPGe) crystals separated by a distance of 0.2 mm from each other. Fig. 3.3.2 shows the general layout of the Clover detector.

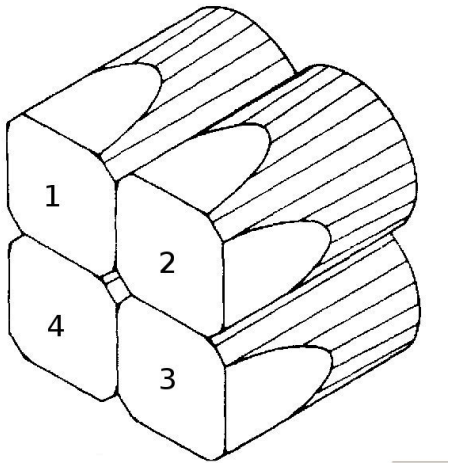

FIG. 3.5: Clover detectors consist of four separate co-axial n-type of HPGe crystals separated by a distance of 0.2 mm. The four crystals have length dimension of 70 mm and a diameter of 50 mm.

These four crystals have a length dimension of 70 mm and a diameter of 50 mm. Each Clover crystal is connected separately to an output electronics, in other words each Clover crystal has its own electronics which leads to independent output signals. The main advantage of the granularity of the Clover detectors is to give more precise Doppler correction and to reduce the broadening of the peaks due to the Doppler effects. Therefore, Doppler broadening gives bad resolution with respect to the angle between the γ-rays and the axis of the emitter. Thus Doppler correction improves the energy resolution when the recoil nucleus is no longer stopped in the target.

The Clover detector can be operated in two different modes, the direct mode and the add-back mode. In the direct mode, each of the four crystals is considered independently as a separate detector. If the number of hit is more than one hit, the full energy peak is considered to be the sum of the individual energy peak of the four segmented crystals and is give by Eq. 3.4 [41],

$$\epsilon_{direct} = \sum_{i=1}^{4} \epsilon_i. \tag{3.4}$$

In the add-back mode, coincidence hits in different crystals are considered and summed

together in order to reconstruct the full energy peak. Conventionally, only horizontal and vertical scattered γ-ray, which are double hit events, can be included in the add-back process. While diagonal of three hit events are assumed to be from more than one coincidence γ-rays and considered to be accidental events [42]. Therefore, the full energy peak in the add-back mode is the sum of one fold events efficiency, two fold events efficiency, three fold events efficiency and four events efficiency and can be written as,

$$\epsilon_{add-back} = \sum_{i=1}^{4} \epsilon_i + \epsilon_{2fold} + \epsilon_{3fold} + \epsilon_{4fold} = F \sum_{i=1}^{4} \epsilon_i. \tag{3.5}$$

where F is the add-back factor is defined as the ratio of the full energy peak efficiency in the add-back mode $(eff_{full})_{add-back}$ to the full energy peak efficiency in the direct mode $(eff_{full})_{direct}$ to measure the improvement of the total full energy peak efficiency [42]. Where the add-back factor F can be given by, $F = (eff_{full})_{add-back}/(eff_{full})_{direct}$ [41].
The relative efficiency for each crystal element is approximately found to be 23 % and the total relative efficiency with add-back is $\sim$ 130%. The add-back is useful by enhancing the ratio of the full energy to partial energy events which is known as the Peak-to-total ratio (P/T) giving Clover detectors the advantage of detecting high energy γ-rays. For example, The measurements in table 3.1 were performed with a ^{60}Co source at a distance of 25 cm from Clover detectors. The total γ-ray spectrum was integrated for three different regions; 50 keV-1345 keV, 100 keV-1345 keV and 200 keV-1345 keV, respectively and the Peak-to-Total ratio is given in Table. 3.1.
The advantages of the Clover detectors can be summarized as follows [43]:

- To reduce the effect of Doppler broadening with increased granularity, thus reducing the opening angles of the Clover crystals.
- Good energy resolution.
- Good timing response.
- Obtain a high sensitivity to the linear polarization of gamma rays because of its four segmented crystals that are acting as polarimeter [44].

Region [keV]	Clover Peak-to-Total ratio	
	without BGO	with BGO
50 - 1345	0.33	0.43
100 - 1345	0.34	0.44
200 - 1345	0.36	0.46

TABLE. 3.1. Peak-to-Total ratio measured with a ^{60}Co source at a distance of 25 cm for individual Clover detector (with add-back) without using the BGO anti-Compton shield and with BGO shield [5].

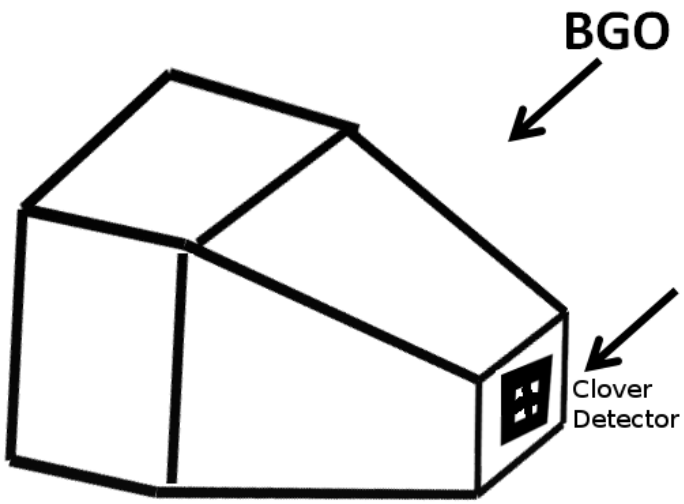

FIG. 3.6. The schematic layout of the BGO Compton suppression shield.

3.3.3 BGO Shield

Bismuth Germanate ($Bi_4Ge_3O_2$) detectors are scintillators detectors with a large atomic number ($Z_{Bi} = 83$) and therefore a high γ-ray stopping power. The BGO is used as a veto detector for Compton scattered events which escape from the HPGe detector volume without having deposited its full γ-ray energy. The energy of the escaped γ-rays is deposited in the BGO scintillator and converted into light photons. Sequentially, the light photons are converted by the photocathode into e^-. The electrons are collected using the photomultiplier and through the photoelectric effect electrons are emitted from the photocathode

as a secondary emission. The number of electrons is amplified in the photomultiplier by accelerating the electrons towards electrodes, which is known as dynodes, by increased voltage. For the electrons to reach the next dynode, secondary electrons are produced, therefore multiplying the signal and the current flows from the anode to ground is directly proportional to the photoelectron flux generated by the photocathode.

3.3.4 Compton Suppression

There are two possibilities for γ-rays to deposit its energy in the HPGe detectors. Either the full energy of the incident gamma-rays deposited or scattered out of the HPGe. When the γ-ray scatters out, it increases the background and therefore, the BGO is positioned around each Clover detector to reduce the background. Fig. 3.6 illustrates the general layout of the BGO shield. The main aim of the BGO ($Bi_4Ge_3O_2$) shield is to veto events with Compton scatter.

3.3.5 Low Energy Photon Spectrometers (LEPS)

Low energy photon spectrometers consist of a single Germanium crystal of p-type. This Ge crystal has a diameter of 60 mm and thickness of 10 mm. Each crystal is segmented into four quadrant. The LEPs are mainly used to detect both γ-rays and X-rays with an incident energy below 200 keV [43, 45].

3.3.6 AFRODITE frame and target chamber

The AFRODITE frame is made of aluminum to support the 16 germanium detectors and retracted from the beam line to allow access to the target chamber. The target chamber as seen in Fig. 3.7 was designed for low absorption and to enable mounting of the target into the target ladder.

The target ladder is positioned inside the target chamber and is usually supports Beryllium oxide beam position monitor usually placed in top position, the target foil in the bottom position while the middle position is used for empty frame for checking and focusing the

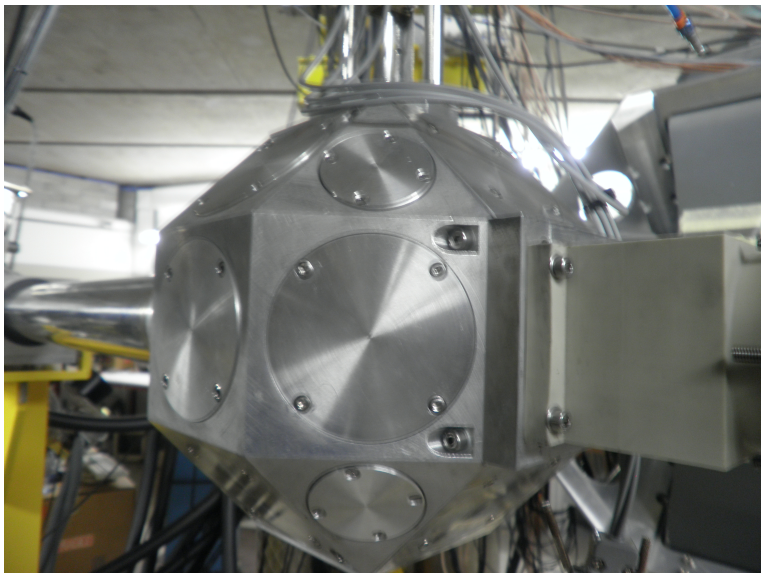

FIG. 3.7. The general view of the AFRODITE reaction chamber.

beam spot.

3.3.7 Target preparation

A natural tantalum target was used for the target preparation. A thin and thick Tantalum targets were used with thickness of $500\mu g/cm^2$ and 10 mg/cm^2 respectively. In this experiment, both thin and thick targets were used in the ^{18}O + ^{18}O reaction. The targets were prepared in the target laboratory of iThemba LABS by oxidizing the tantalum foil using the hydrolysis process. The Ta foil was dipped in a container filled with ^{18}O enriched water and connected to the positive pole of a variable voltage power supply (0 - 300 V). A 1 cm^2 cathode is placed in front of the Ta foil at a distance of 1 cm in the container. A voltage of 200 V is applied for about 10 mm which is a sufficient time to dissociate enough H_2O molecules, and the oxidation of Ta to take place.

3.3.8 DIAMANT Detector

The DIAMANT detector array is a 4π scintillation detector for detecting light charged particles consisting of 84 CsI(TI). Each detector is made of a CsI(TI) Scintillation crystal

with 3 mm thick, a Plexiglas light guide and a PIN photodiode. The DIAMANT detectors were established to work as an ancillary detector inside large γ-ray spectrometers, such as EUROGAM, EUROBALL, EXOGAM and AFRODITE [46]. The DIAMANT is a rhombicuboctahedron consists of 84 with 3mm thickness of CsI(TI) scintillators with photodiode readout [3], 76 pcs with 14.5mm thickness of squared-like-shape and 8 pcs with a thickness of 29mm of triangle-like-shape as shown in figure 3.8.

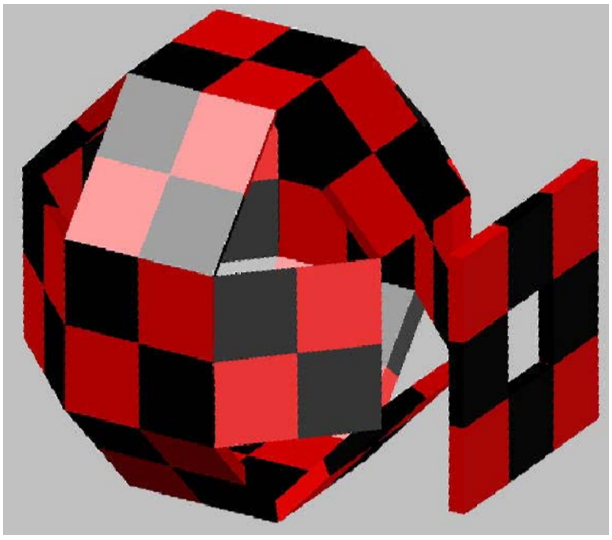

FIG. 3.8. The general layout of DIAMANT detector array [3].

In this experimental investigation, DIAMANT was implemented inside the AFRODITE γ-spectrometer array at iThemba LABS in slave mode. The detected light charged particles increase the γ-ray selectivity by gating on the emitted light charged particles.

DIAMANT Geometry

The geometry of DIAMANT is build as Rhombicuboctahedron. It consists of a flexible PCB forward wall detectors known as the Chessboard. The Chessboard has two possible dimensions either 3×3 or 5×5 detectors as illustrated in Fig. 3.8. The DIAMANT detector consists of a Chessboard in the forward angles of the detector. The Chessboard is a 3×3 detector where the middle detector is removed in order to enable the beam to pass through as described in Fig. 3.8.

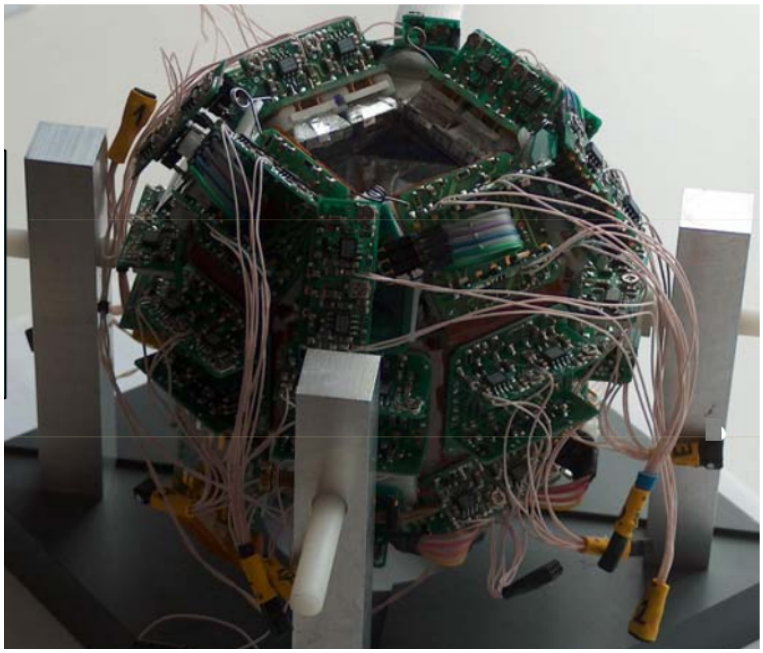

FIG. 3.9. The inner structure of DIAMANT including the Electronics [3].

Particle Identification Method of DIAMANT

The main features of the DIAMANT charged particle detector is the particle identification with the particle energy measurement and the time reference information. For the determination of the particle type, a pulse shape discrimination techniques is used [47]. This plus shape discrimination technique is based on the fact that for these scintillation crystals, the scintillation constants depend on the type of the particle [48]. Thus more light will be emitted when α particles deposit their energy than protons because the energy loss depends basically on the A, Z of the particle. The particle discrimination is performed using the rise time of the signal (Fast component) and the decaying part of the signal (Slow component) [49, 46]. Thus, the particle identification of DIAMANT is the ratio of the fast component of the signal (leading edge) over the slow component (decaying part of the signal) when p, d, t, α particle deposit their energy on the crystal. Fig. 3.10 shows a typical signal output from a CSI detector.

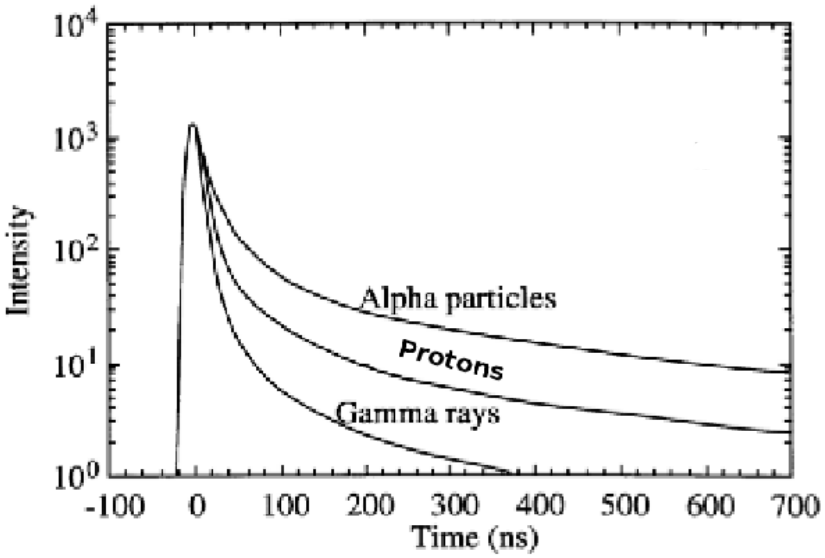

FIG. 3.10. Signal output from CSI detectors illustrating the decay time of different particles and is used for the discrimination between particles [4].

DIAMANT Efficiency

The geometrical efficiency of DIAMANT detector and the efficiency of detecting charged particles is given in Table 3.3.8[3].

Type	**Efficiency %**
geometrical efficiency	$\sim 90\%$
detection of protons	$> 70\%$
detection of α particles	$\approx 50\%$

TABLE. 3.2. Geometrical and detection efficiency of DIAMANT detector.

The proton efficiency is different from the efficiency of α particle due to the absorbers placed in front of the CsI detectors of DIAMANT. Therefore, the particle detection efficiency will depend on the particle energy loss into the absorbers.

3.4 Data Acquisition System

In this section, both AFRODITE and DIAMANT electronics for signals processing are discussed.

3.4.1 AFRODITE electronics

In the AFRODITE setup, different data acquisition are used to process signals from the detectors. Using the Standard Nuclear Instrumentation Module (NIM) and the Computer Automated Measurement and Control (CAMAC) which are located in the AFRODITE vault to process signals from the Clover and LEPs detectors. The signals from the Clover detectors are processed by the RIS modules. These RIS module [50] have integrated circuits including the standard fast-slow processing and the anti-Compton veto of events with a BGO signal in order to produce clean signals from the Ge detectors [50]. The signals then feed to the trigger units where for this experiment is required two coincidence events when two Clover detectors fired. Once the trigger signal is generated it informs the ADCs, TDCs and the RIS modules in order to convert time and energy signals to digital signals. The ADCs and TDCs of the RIS module are readout by a VME module known as F2VB, then the data is stored to Linux environment workstation to write the data on tapes and for later offline/online analysis. The Multi Instance Data Acquisition System (MIDAS) [51] is used for data sorting. For the DIAMANT data readout, the VXI card environment is used to process the signal from the CsI(TI) scintillation detectors. In the following section (Sec.3.4.2), the VXI card is discussed in more detail.

3.4.2 DIAMANT electronics

The DIAMANT array is used to measure the coincidence events detected by its CsI(TI) with the AFRODITE γ-rays using the VXI electronics set up which is controlled by a Master Trigger Unit (MTU). This Master Trigger Unit produces two global trigger signals. The first trigger signal is called the Fast Trigger (FT) and the second trigger signal is called the Validation (VAL) signal.

Both trigger signals are deduced from the Ge detectors of the AFRODITE. The Fast Trigger (FT) is representing a first-level trigger, where the VAL signal provides a second-level trigger. The trigger signals are connected to all channel so that the local trigger decides whether the channel itself is part of the coincidence event marked by the fast trigger. Data readout happen only when the VAL signal is delivered.

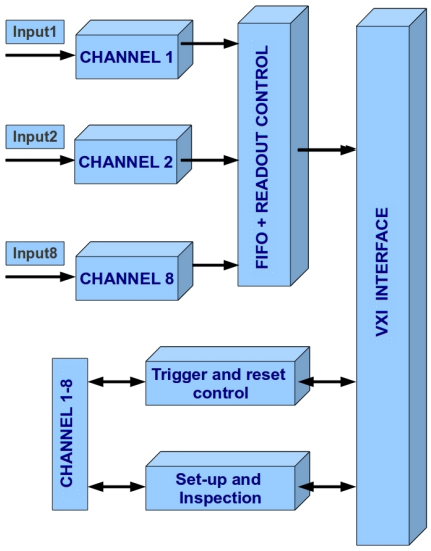

FIG. 3.11: Block diagram of the VXI card.

Fig. 3.4.2 describes the block diagram of the VXI card which is developed for the DIAMANT array in Debrecen. The VXI card contains eight channels, each channel generates three information: the particle energy, the PID and a time reference which is the time relation between the signals arriving from the particles detectors and the γ-rays. The data obtained from the different channels are processed to the FIFO+READOUT CONTROL and therefore delivered to the VXI interface through a 32 bit bus [46]. One VXI card consists of two Serial ADC Readout Controllers (SAROC) where ADC stands for Analog Digital Converter. The main function of the SAROC is to control the channels [46].

Chapter 4

Experiment and Data Analysis

In this chapter the experimental arrangement and the procedures of the data analysis are discussed.

4.1 The Experiment

The experiment was performed during two running weekends in order to collect enough data. Oxygen-18 ions were produced in the Electron Cyclotron Resonance ion source (ECR) then pre-accelerated by the Solid Pole injector Cyclotron2 (SPC2) and accelerated to the desired energy with the Separated Sector Cyclotron (SSC) at the iThemba LABS facility illustrated in Fig 4.1 and Table. 4.1.

From the accelerator, the beam can be steered into different sections for different experiments through the X, P1, P2 and S beam lines as described in Fig.4.1 [52]. The beam was delivered to the AFRODITE γ-ray spectrometer vault as denoted by the symbol F in Fig. 4.1.

4.2 Data Processing

During the experimental run, the data stream was saved in order to be processed off-line for data analysis. The off-line data analysis was performed using the ROOT [53] package.

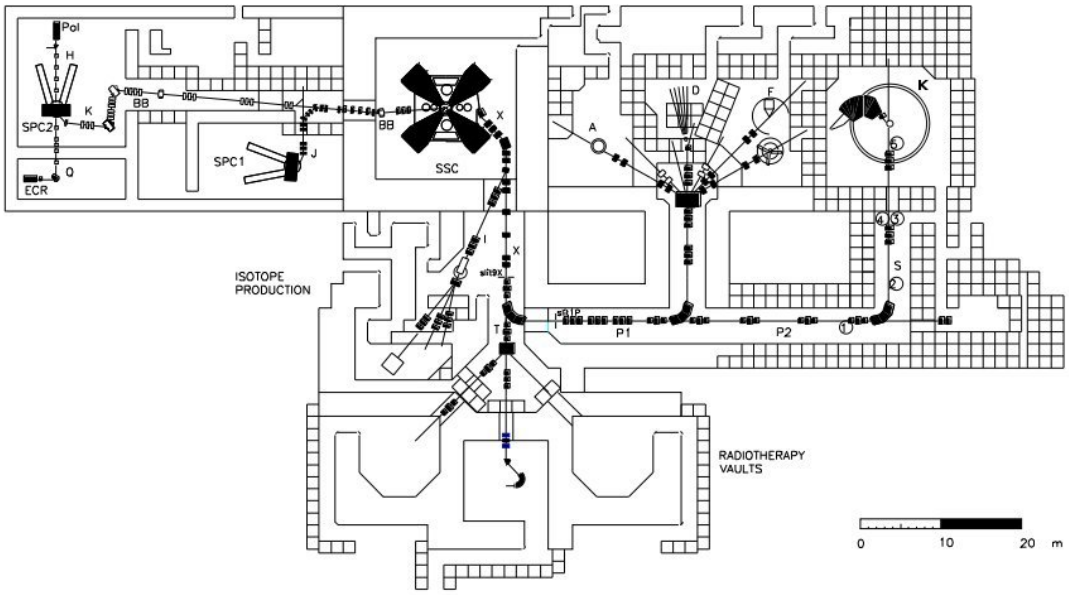

FIG. 4.1. A plane view of the cyclotron facility at iThemba LABS.

Abbreviation	**Description Details**
A	Scattering Chamber beam line
D	Collimated neutron beam facility
ECR	Electron Cyclotron Resonance ion sources
ECD	Electron and Cable Distribution
F	AFRODITE γ-ray spectrometer
K	K600 magnetic spectrometer
IP	Isotope Production
L	Low energy experimental area
P	Polarized ion source
SPC1	Solid pole injector cyclotron for light ions
SPC2	Solid ion cyclotron for heavy and polarized ions
SSC	Separated Sector Cyclotron
TC	Isocentric system for neutron therapy
TR	Horizontal beam line for proton therapy
TL	Beam lines for proton

TABLE. 4.1. Description of the iThemba LABS facility as depicted in Fig 4.1 [6].

ROOT is an object-oriented framework used C++ programming as interpreter which is used as command lines and script processor. The data analysis code is called SimSort [54]

which is an acronym of Simulation and Sorting code. The SimSort code converts data from Multi Instance Data Acquisition System (MIDAS) into ROOT files. The advantage of ROOT data base files is to simplify the data analysis procedures by populating the data into histograms and ROOT trees as TTree data structure where the energy, time and position information of each detected particle are stored as well as particle identification when applicable and other pre-calculated parameters.

4.3 Energy Calibration of the Ge Detectors of AFRODITE

The calibration data were obtained at the beginning of the two weekends of the experiment. Using a ^{152}Eu source, single γ-ray events were recorded and were used to calibrate the clover detectors of the AFRODITE γ-ray spectrometer. A typical γ-ray spectrum for the ^{152}Eu source is shown in Fig. 4.2 with energy lines from 122 to 1408 keV.

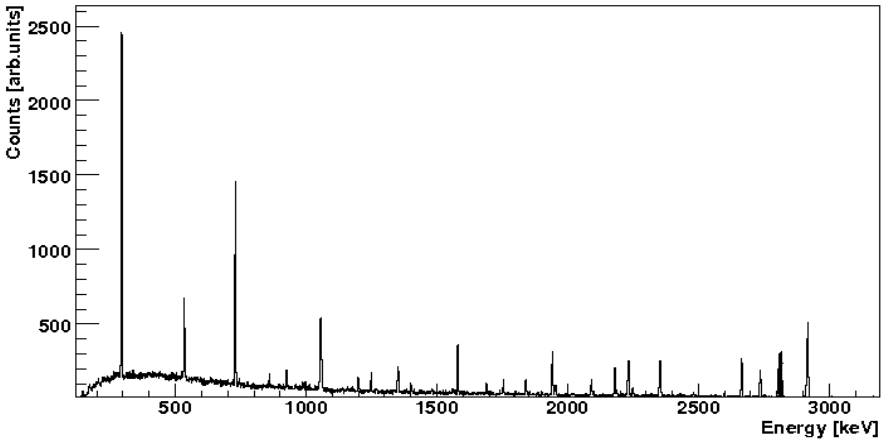

FIG. 4.2. Uncalibrated γ-ray spectrum of a ^{152}Eu source obtained from the Clover detectors.

For the Ge calibration, a C++ code was written within the ROOT framework for automatic calibration. The known γ-lines of ^{152}Eu are identified in the uncalibrated spectrum as shown in Fig. 4.2; The centroid of each peak is obtained from a Gaussian fitting and a linear background subtraction. The fitting function, to extract the peak centroids, is a combination of a polynomial function of order 1 and a Gaussian function and can be written as in Eq. 4.1

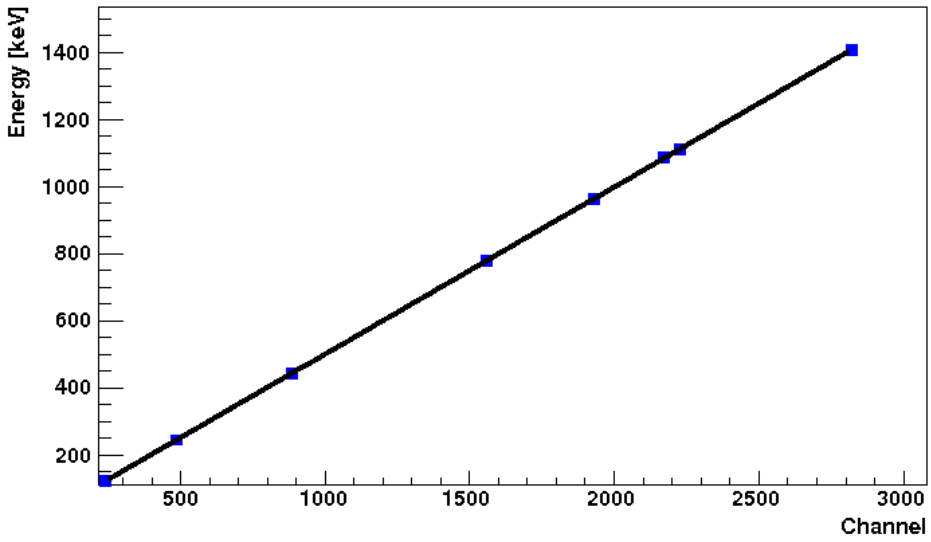

FIG. 4.3. Linear energy calibration of the Ge detectors of the AFRODITE obtained from the ^{152}Eu spectrum and using a C++ code for the linear fit of the peaks.

$$f(x) = A + Bx + \frac{C}{\sqrt{(2\pi\sigma)}} e^{\frac{-(x-D)}{2E}} \tag{4.1}$$

where A, B are parameters defining the background and C, D are parameters defining the peaks of the γ-ray spectrum for the ^{152}Eu source and $2.35\times\sigma$ is the Full Width at Half Maximum (FWHM). The energy calibration is obtained from a linear fit.

4.4 Energy Calibration of DIAMANT

For the DIAMANT calibration, an accelerated ^{16}O with $E_{lab} = 53$ MeV was impinging on a ^{12}C target of 500μg/cm^2 thickness placed in the middle of a calibration mask depicted in Fig. 4.4. The compound nucleus ^{28}Si is populated with high excitation energy $E_x =$ in fusion reaction. Therefore, ^{28}Si decays to ^{24}Mg via α particle emission carrying the energy difference between the excitation energy in ^{28}Si and the Q-value of the decay thus defining the kinetic energy of the α particle. The populated ^{28}Si nucleus is moving therefore the energy of the emitted particle depends on the emission angle θ. The proton, produced in the ^{1}H(^{16}O,^{1}H) elastic scattering reaction, and α energy are plotted as a function of the angle θ as illustrated in Fig. 4.7, and Fig. 4.6. Before the delivery of the beam into the

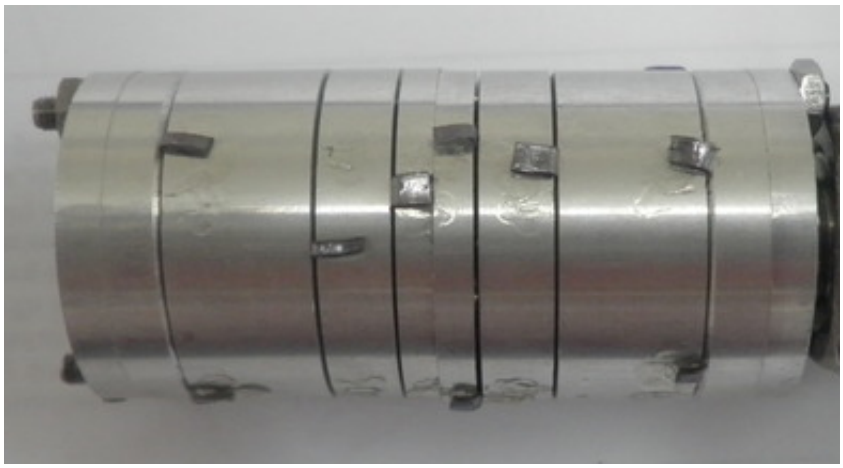

FIG. 4.4. Calibration mask cut into eight washers separated by a distance of 0.2 mm to keep the washers apart. A 500 μg/cm^2 Carbon target is placed between the two middle washers.

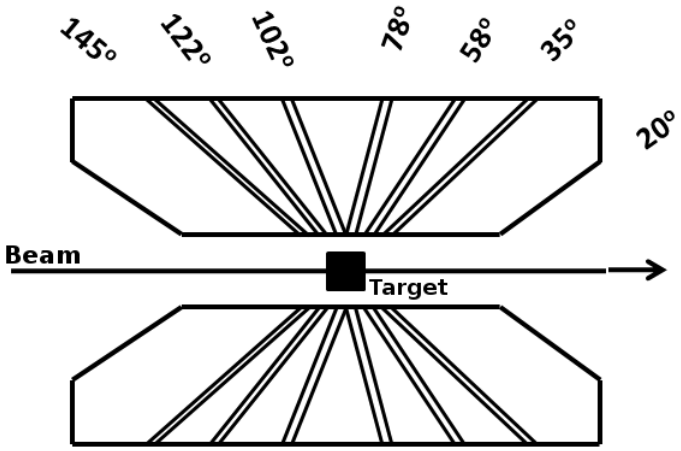

FIG. 4.5. Drawing to illustrate the calibration mask cut into eight washers separated by a distance of 0.2 mm to keep the washers apart. The reaction takes place in the center of the calibration mask where the target is situated. Only particles passing through the space at the indicated angles will be detected by DIAMANT.

target. Absorbers made from Ta are placed in front of the CsI(Tl) detectors to absorb the scattered ^{18}O from ^{181}Ta target towards the detectors. The thickness of the absorbers was 20 μm in the front wall and the first two rings in the forward angles. In the remaining rings, 15 μm absorbers were used and the energy loss of proton, deuteron, triton and α particles on the absorbers were calculated in Table. 4.2 using the SRIM code [55]. The

calibration mask was made of aluminum and cut into eight washers with an angle in order to select precise angles as shown in Fig. 4.4. The space between the washers was 0.2 mm in order to keep the opening angle $\delta\theta$ <1°. The calibration mask was placed in the center of the target chamber in front of the six rings of the DIAMANT detectors.

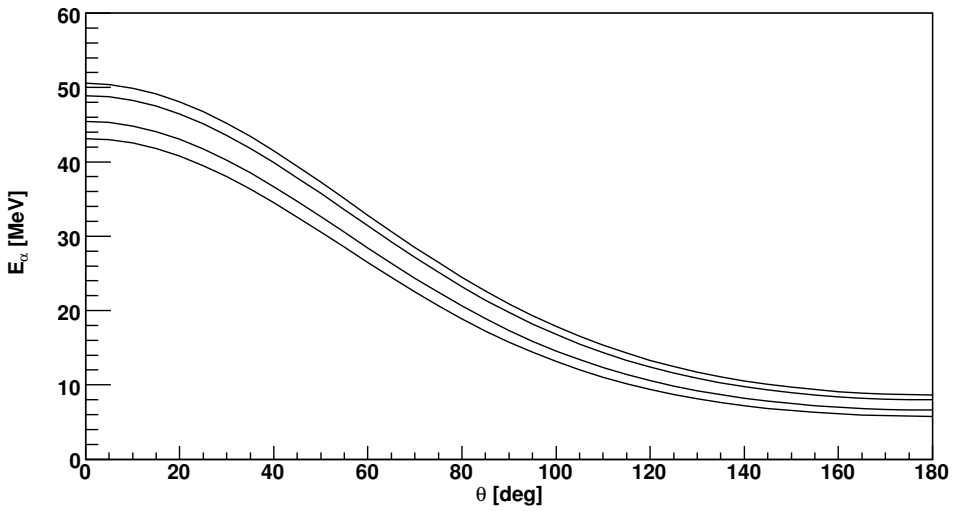

FIG. 4.6. The α particles are produced in the ^{12}C(^{16}O,α)^{24}Mg reaction at $E_{lab} = 53$ MeV. The α particle energy is obtained as a function of the emission angle. The energy states of ^{24}Mg correspond from top to bottom to the ground state, 1368.7 keV, 4122.8 keV and 6010.8 keV excited states.

Incident E [MeV]	ΔE_p	ΔE_d	ΔE_t	ΔE_α
5	0.8	1.2	1.4	5
10	0.5	0.8	0.9	5.2
20	0.3	0.5	0.8	3.5
40	0.2	0.3	0.5	1.8

TABLE. 4.2. Energy loss in MeV of different particles in Ta absorbers with a thickness of 15 μm.

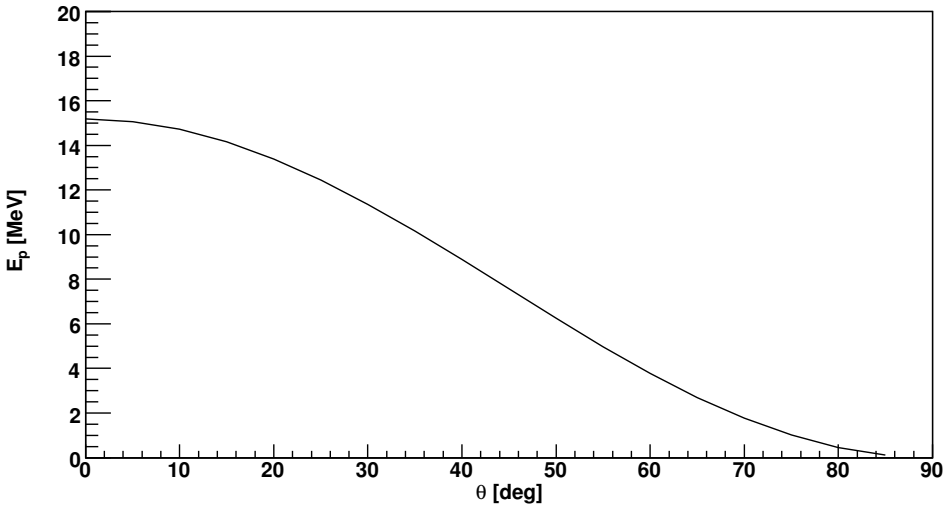

FIG. 4.7. Proton energy as a function of the emission angle in the ^{1}H(^{16}O,^{1}H) reaction at $E_{lab} = 53$ MeV.

4.4.1 Particle identification of ^{16}O + ^{12}C

From the ^{16}O + ^{12}C reaction at $E_{lab} = 53$ MeV, protons and α particles were identified using the particle identification methods as discussed in Sec. 3.3.8. From the offline data

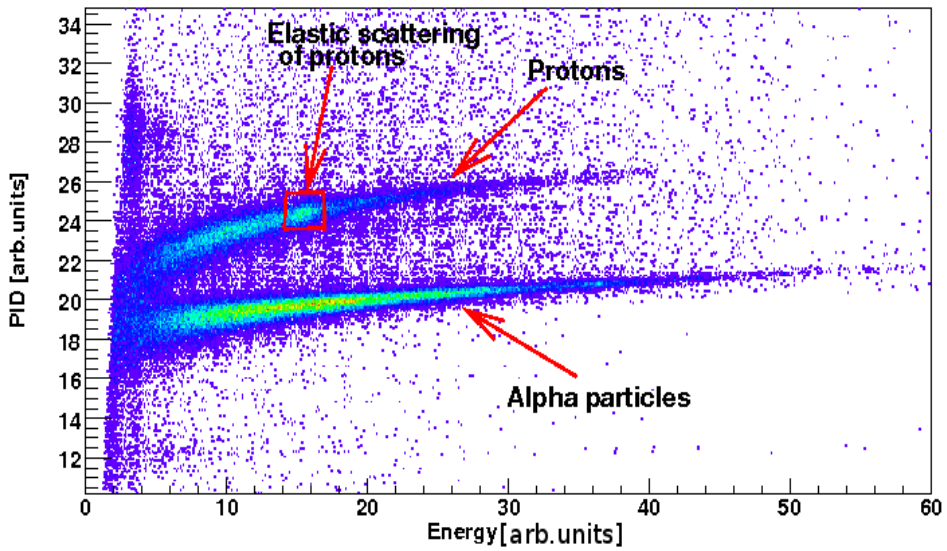

FIG. 4.8. PID spectrum obtained from the ^{16}O + ^{12}C reaction at 53 MeV.

analysis a PID spectrum is obtained from the calibration data as illustrated in Fig. 4.8. In order to calibrate the particle energy spectrum, appropriate gates select the protons and the α particles. Therefore, the energy spectra gated on protons and α particles are obtained in Fig. 4.9 and Fig. 4.10 respectively. In the energy spectrum gated on proton, the strong peak is identified as the elastic scattering of proton due to water contamination on the target. Therefore, the elastic scattering of proton in the ^{1}H(^{16}O,^{1}H) reaction is observed. The energy of the scattered protons depend on the scattering angle, where the limit angle for protons is 90°, and is used to calibrate the DIAMANT detectors at forward angles.

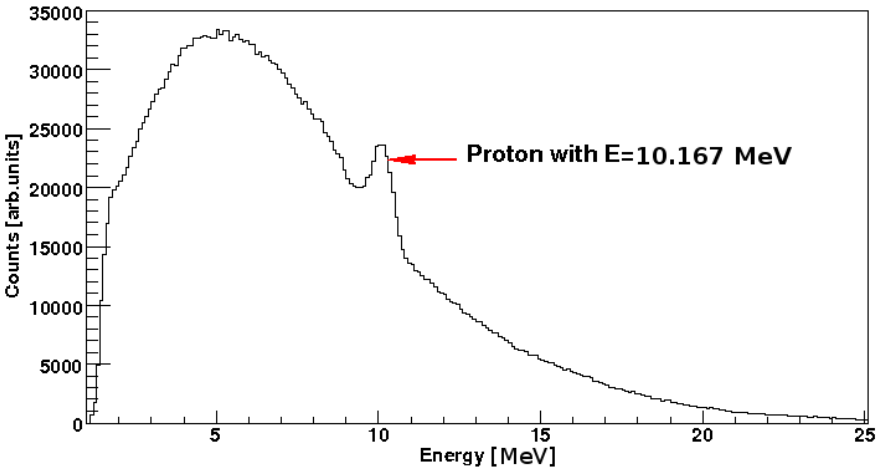

FIG. 4.9. Proton spectrum gated on the PID obtained from the ^{1}H(^{16}O,^{1}H) reaction.

Similarly, in the energy spectrum gated on α particles the structure is assigned to the ground state, 1368.7 keV and 4122.8 keV excited states, as described in Fig. 4.10, of ^{24}Mg populated from the ^{16}O + ^{12}C reaction at $E_{lab} = 53$ MeV.

In the forward detectors the ground state and the first excited state of ^{24}Mg are resolved from each other, which is not the case at larger angles where they overlap. Using the energy of the α particles, originating from the decay of ^{28}Si, calculated at each angle by the computer code CINEQ [56], a calibration is performed for the DIAMANT detectors. The detector response of CsI(Tl) scintillators is a non-linear with the deposited energy, especially for heavy ions. Therefore, the calibration points for α particle were taken at high energy.

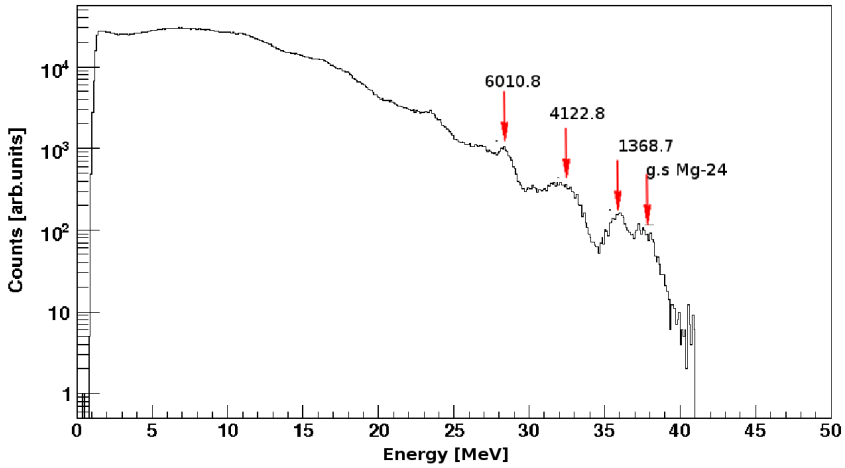

FIG. 4.10. α particle spectrum gated on the PID obtained form the $^{12}C(^{16}O,\alpha)^{24}Mg*$ reaction.

PID matching of the DIAMANT detectors

In order to match the PID signal of all the DIAMANT detectors, a gate is placed at 20 MeV as shown in Fig. 4.11. By setting a condition at E_α = 20 MeV ±1 MeV the PID spectrum is projected as given in Fig. 4.12 where two narrow peaks are identified as α and proton. Therefore, the PID gain was set arbitrarily in order to match the α and proton PID at 20 [arb.units] and 25 [arb.units], respectively.

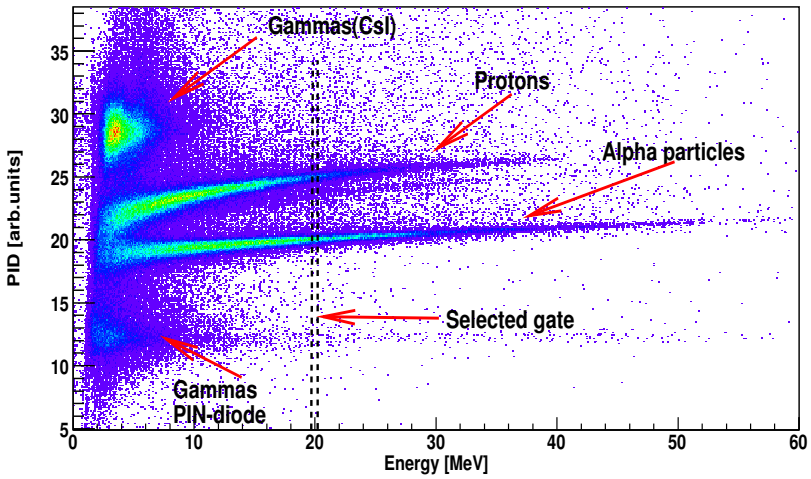

FIG. 4.11. Gate on the PID spectrum at E_α = 20 MeV ± 1MeV.

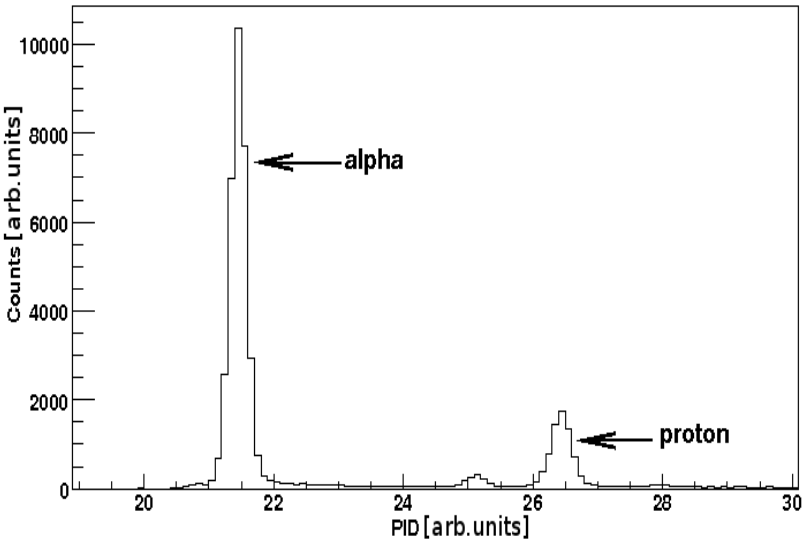

FIG. 4.12. Projection on the PiD signal.

4.5 Data analysis of $^{18}O + ^{18}O$

Using the particle identification method described in section 3.3.8, particles detected in the $^{18}O+^{18}O$ reaction were identified as shown in Fig. 4.13

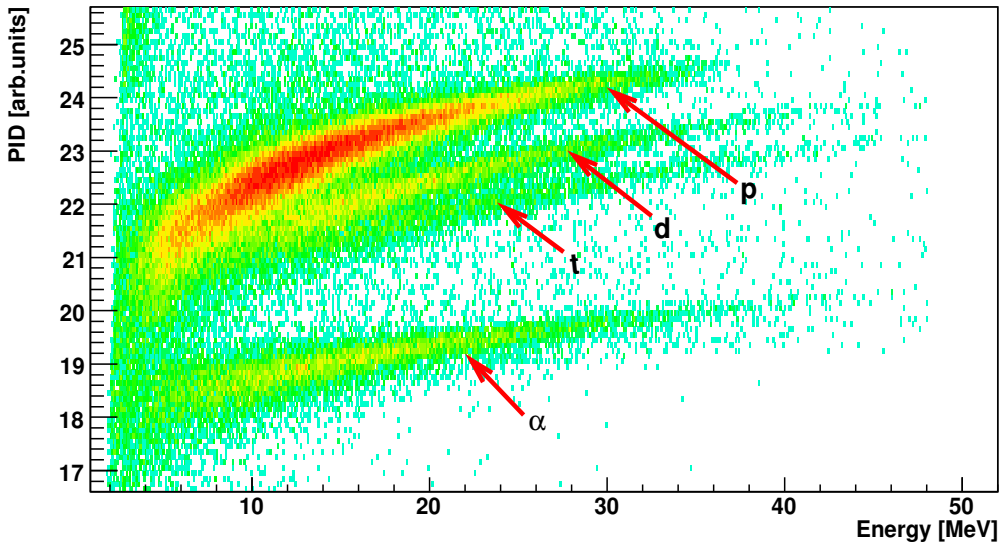

FIG. 4.13. Particle identification in the $^{18}O + ^{18}O$ reaction at $E_{lab} = 65$ MeV.

From Fig. 4.13 proton, deuteron, triton and α particles were detected in the ^{18}O + ^{18}O reaction at $E_{lab} = 65$ MeV. The emission of these different particles is due to high excitation energy of the ^{36}S compound nucleus to populate P and Si residual nuclei through the evaporation of light particles. To isolate P and Si nuclei populated in various channels, a selection of proton, deuteron, triton and α particles is made by setting gates on these particles in the PID spectrum with identification of the residual nuclei via γ-ray. The gates in which to select the detected particles are shown in Fig. 4.14

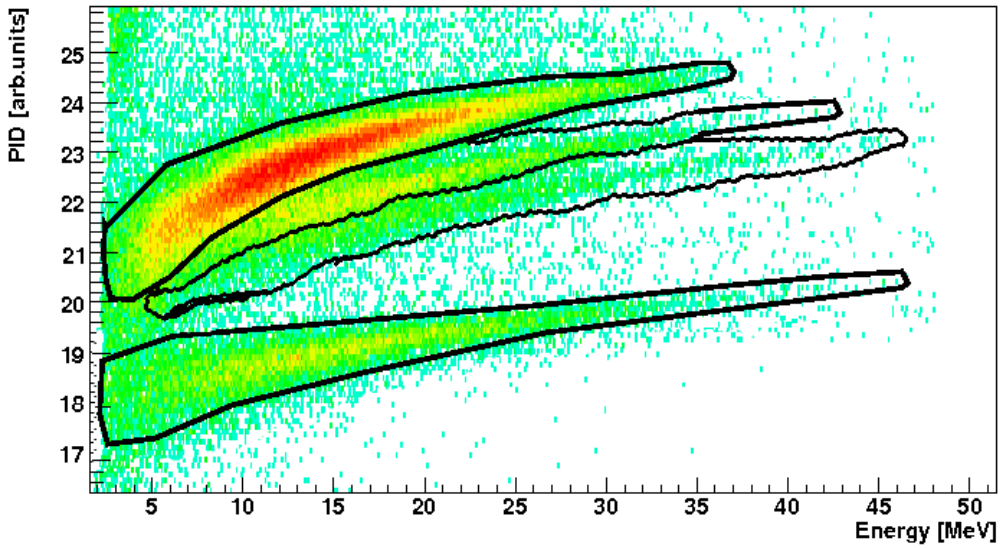

FIG. 4.14. Proton, deuteron, triton and α particle gates on a 2D PID spectrum.

After setting gates on the proton, deuteron, triton and α particles, total projection of coincident γ-γ-rays are extracted with additional time selections. Fig. 4.15 and Fig. 4.16 show the total projection of the γ-γ-rays after gating on the selected particles.

4.5.1 Identification of the residual nuclei

Due to the large v/c ratio (β), the Doppler shift is expected to be large (4.8% at 45° and 135°). Due to the short lifetime and deviation of the residual nuclei in the target, their direction and velocity information is partly lost at the time the γ radiation is emitted. Moreover, the opening angle of the Ge detectors ($d\theta = 15$) is relatively large. Therefore, Doppler broadening is expected since the uncertainty on θ in the Doppler shift equation is

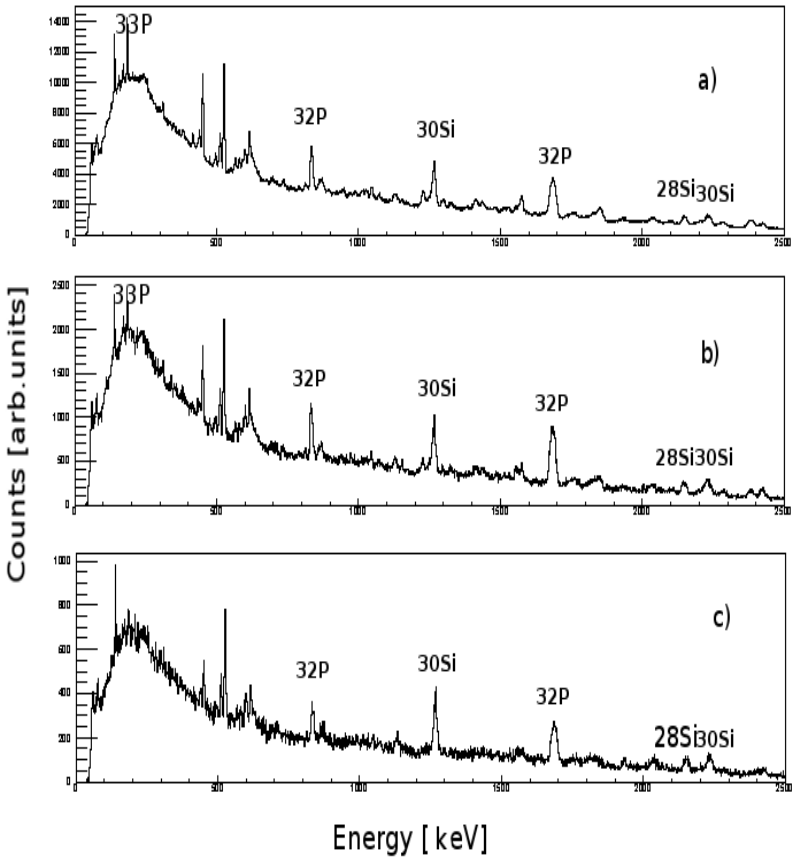

FIG. 4.15. Total projection of γ-rays gated on proton (a), deuteron (b) and triton (c).

large. The γ spectra of ^{30}Si, ^{32}P are Doppler corrected but the best resolution achievable at 1256 keV is 51.04 keV. This resolution is relatively poor compared to approximately 2.0 - 2.5 keV resolution (FWHM) obtained at 1332 keV with a ^{60}Co radioactive source. As a consequence most of the residual nuclei populated in the reaction could not be identified due to a lack of resolving power. The strongest channels are predicted to populate ^{32}P, ^{29,30}Si, with 47.9 mb, 54.6 mb and 88.6 mb respectively from the CACARIZO code. The cross section can not be determined accurately with the present data but those channels are identified as the most intense.

From the total projection of γ-rays gated on proton, deuteron, triton and α particles described in Fig. 4.15, 4.16, a number of residual nuclei are identified. The identification of the main transitions was made by setting gates on known energies to isolate specific evaporation residues. Firstly, a gate was placed on protons and E_γ =823-849 keV then the

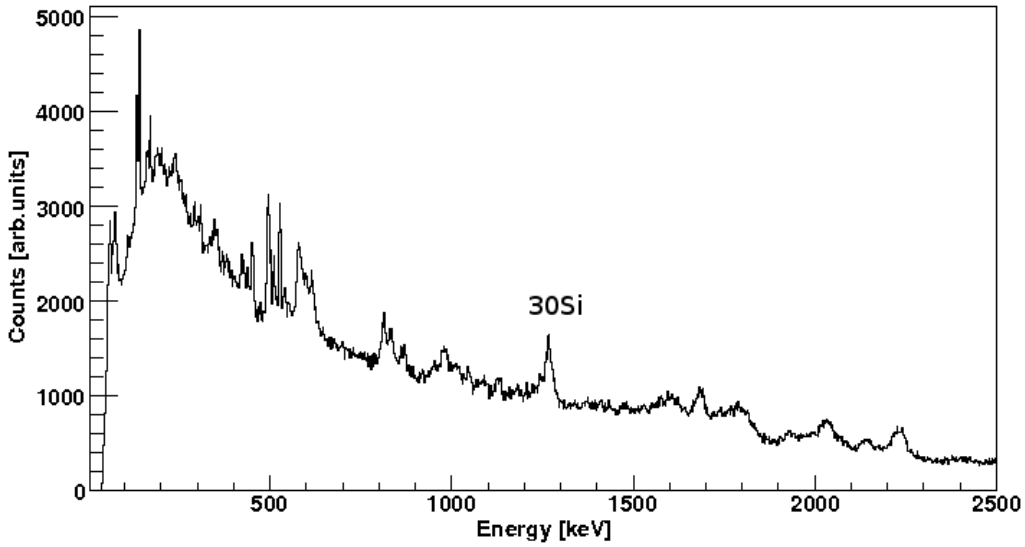

FIG. 4.16. Total projection of γ-rays gated on α particles.

total projection was obtained as illustrated in Fig. 4.17. From Fig. 4.17, the 1679 keV

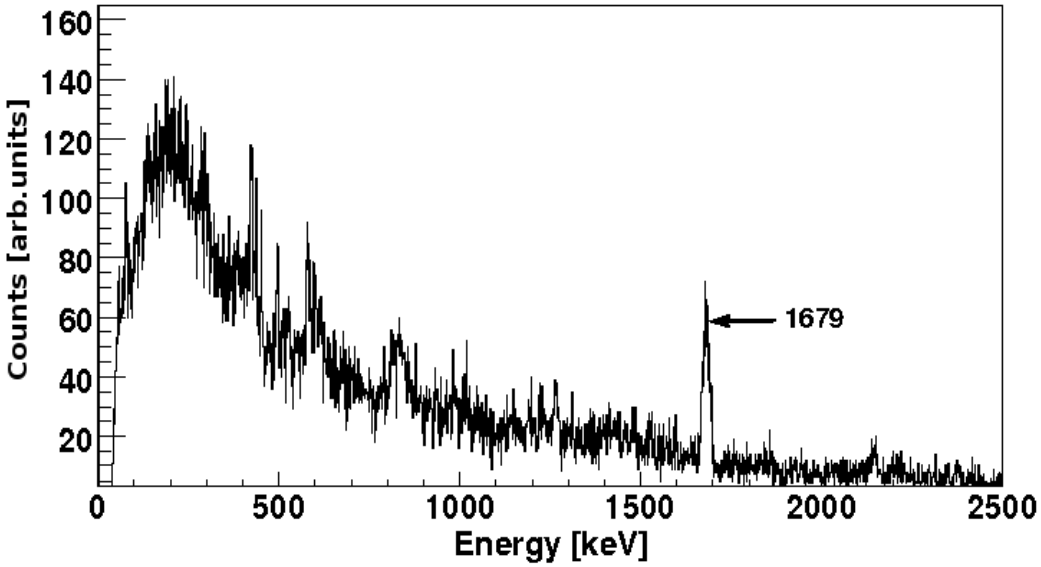

FIG. 4.17. γ-rays spectrum gated on 1p and 823-849 keV of ^{32}P. The 1679 keV is the combination of the 1679.9 keV and 1687.9 keV transitions.

comes in coincidence with 836 keV and assigned to ^{32}P nucleus with informations on the intensity, spin and parity of the two coincident γ-rays of the adopted level as illustrated in

Table. 4.4 [57].

Also, a gate was placed on protons and E_γ = 1239-1286 keV γ-ray yields the spectrum displayed in Fig. 4.18.

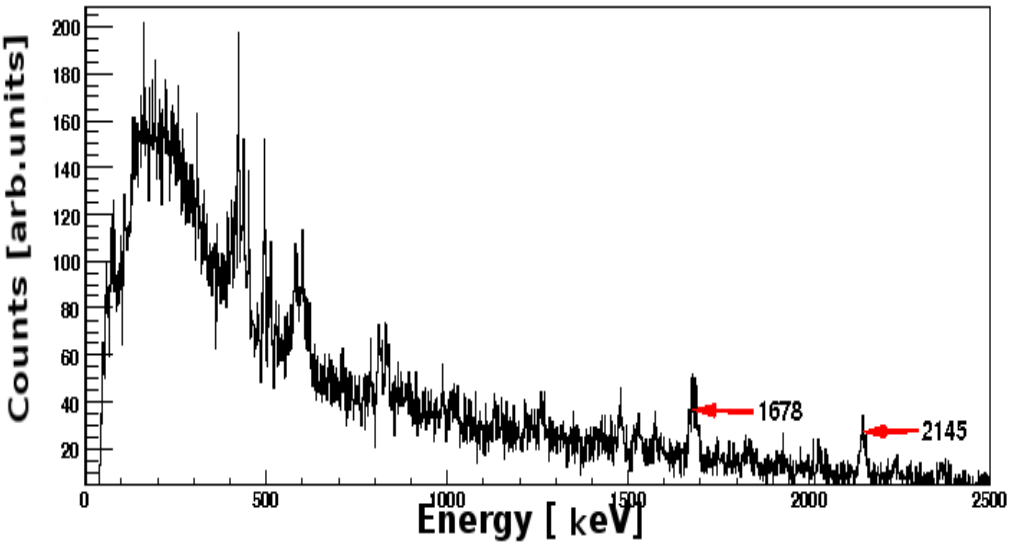

FIG. 4.18. γ-rays spectrum gated on 1p and 1239-1286 keV of ^{30}Si.

The 2142 keV comes in coincidence with 1239-1286 keV, therefore, the two coincident γ-rays were assigned to ^{32}P nucleus. Table. 4.3 gives the information of the adopted level of ^{32}P nucleus including the γ energies, intensity and the branching ratio of the two γ-rays.

E_{γ_1}	$I_{\gamma 1}$	J_i	E_i	E_{γ_2}	I_{γ_2}	J_i	E_i	Branch(%)
1266.10	10.00	$\frac{3}{2}^+$	1266.1	2148.60	7.54	$\frac{7}{2}^+$	3414.7	100

TABLE. 4.3. Information of the adopted level of two coincident γ-rays of ^{30}Si.

Furthermore, by gating on proton and 2129-2174 keV, the $\gamma - \gamma$ coincidence projection is given in Fig. 4.19.

Therefore, the two coincident γ-rays are assigned to ^{32}P , according to the energies of the adopted level of ^{32}P nucleus. Also, by gating on deuteron and 1659 - 1712 keV, a coincident spectrum was obtained and described in Fig. 4.20. The coincident γ-rays are assigned to

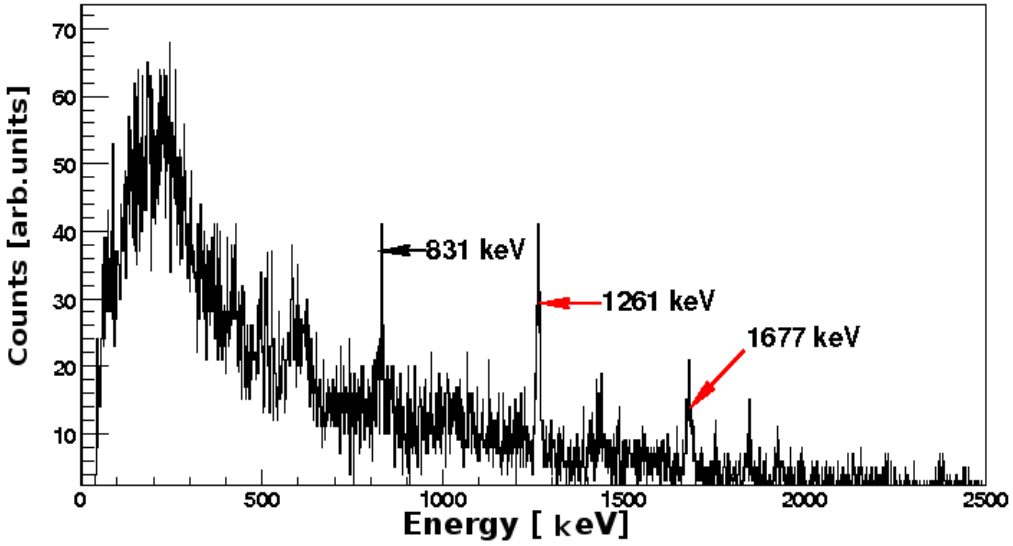

FIG. 4.19. γ-rays spectrum gated on 1p and 2129-2174 keV of ^{32}P.The 1677 keV is the combination of the 1679.9 keV and 1687.9 keV transitions.

^{32}P with the informations given Table. 4.4 containing the intensities, spins and parities of the adopted levels.

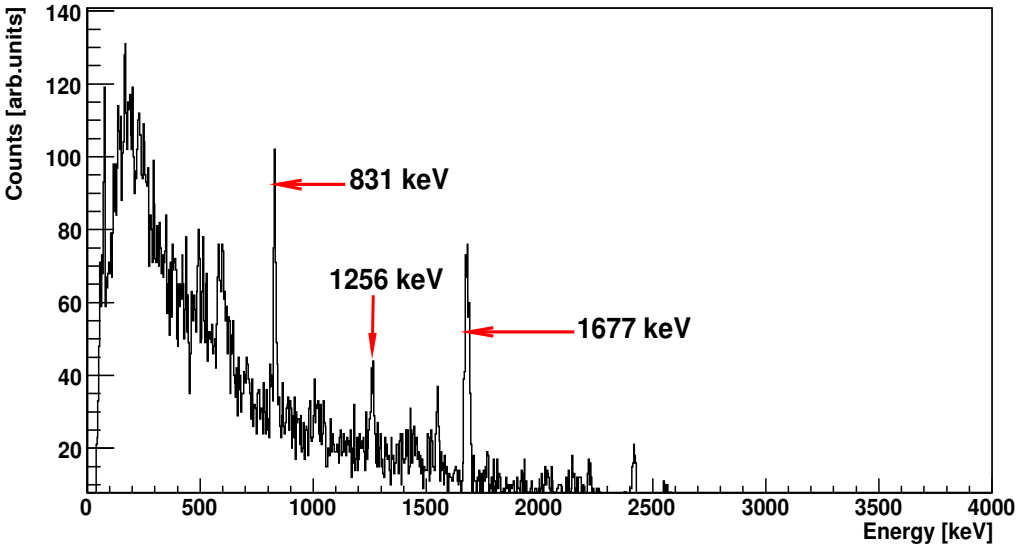

FIG. 4.20. γ-rays spectrum gated on 1d and 1659-1712 keV of ^{32}P.

E_{γ_1}	I_{γ_1}	J_i	E_i	E_{γ_2}	I_{γ_2}	J_i	E_i	Branch(%)
1687.90	10.00	4^-	3443.0	832.10	10.00	5^-	4275.2	93.98
1687.90	10.00	4^-	3443.0	1253.90	10.00		4697.0	93.98
1687.90	10.00	4^-	3443.0	1676.89	10.00	3^+	1755.0	94.98

TABLE. 4.4. Informations of the adopted levels of the γ-rays of ^{32}P.

Chapter 5

Simulation

In this chapter, the SimSort program for simulating and analyzing of the experimental data from nuclear physics experiments is discussed as well as the simulation of the fusion evaporation of the ^{18}O + ^{18}O reaction at $E_{lab} = 65$ MeV.

5.1 The SimSort Code

SimSort is a simulation code used to generate data using identical configurations for both simulations and for data analysis. The code is used to analyze data from nuclear physics experiments. The code is mainly used to simulate and analyze data from coincidence measurements, γ-ray, neutron and charged particle spectroscopy. The SimSort program takes any type of data format such as an event-by-event file and convert it into ROOT trees. The SimSort program is basically used to determine the efficiencies, resolution as well as is used for the kinematic reconstruction, Doppler corrections, particle identifications and all the requirements for nuclear physics experiments. The simulation of the resolution and the efficiency of an experimental setup is performed using the computer code SimSort by taking into account the definition of all the parameters of the experimental setup such as the calibration and the detectors definition. The detectors detail such as the calibration parameters, the threshold, positions of the detectors and the definition of the detectors geometry are considered. The simulation is useful for preparing of new experiments and can be used to optimize the position of the detectors. Beside the simulation of the resolution

and the efficiency, Doppler shift broadening can also be simulated using SimSort where the Doppler corrections can be enhanced and optimized by adjusting the target thickness and the solid angle of the detectors. For Doppler correction, the distance, size and efficiency of the γ-ray detectors are given to the SimSort. Simulated raw data can be generated by applying the same triggers as set in the experimental conditions which allow to simulate not only the reaction of interest but also all the possible type of contaminations. Simulated and experimental raw data can be analyzed in the same way for comparison, embedding or deconvolution [58].

5.2 CASCADE calculations of the ^{18}O + ^{18}O reaction

Fusion evaporation and fusion-fission reactions are simulated by considering a compound nucleus formation followed by its de-excitation. In such a case, the angular distribution of the particles emitted in the center-of-mass frame is expected to be isotropic. A statistical model calculation code such as CACARIZO [12], the Monte Carlo version of CASCADE, is used. The advantage of using CACARIZO is to enable the comparison between experimental and simulated energy spectra. A typical result from the CACARIZO code is the calculation of the cross section of the production of the residual nuclei in fusion evaporation reaction ^{18}O + ^{18}O reaction at $E_{lab} = 65$ MeV, which is given in Table.5.1.

The cascades calculated in this code are recorded in an event-by-event basis and later read by SimSort to convert the events from the center of mass frame to the laboratory frame according to the experimental conditions.

5.2.1 Charged Particle Identification

In the SimSort program, there are different methods for particle identification such as the $\Delta E - E$ method which obtained using double or triple telescopes, the time-of-flight or pulse shape analysis methods. The type of detectors that can be used in the particle identification are the Silicon Surface Barrier Detectors, Position Sensitive Silicon-Strip Detectors (PSSSD), annular detectors and thick scintillator detectors [58]. Therefore, the reaction has to be defined in the input file so that SimSort can reconstruct a missing particle

Mass \ Number	S	P	Si	Al	Mg
34	0.4	0.4			
33	14.3	23.6	0.4		
32	5.3	47.9	4.2		
31		2.9	5.3		
30			88.6	7.3	
29			54.6	14.5	
28			2.4	0.3	
27				17.1	11.3
26				11.3	

TABLE. 5.1. Cross sections of the residual nuclei in mb assuming a total cross section of 300 mb [1, 2] obtained using a Monte Carlo simulation.

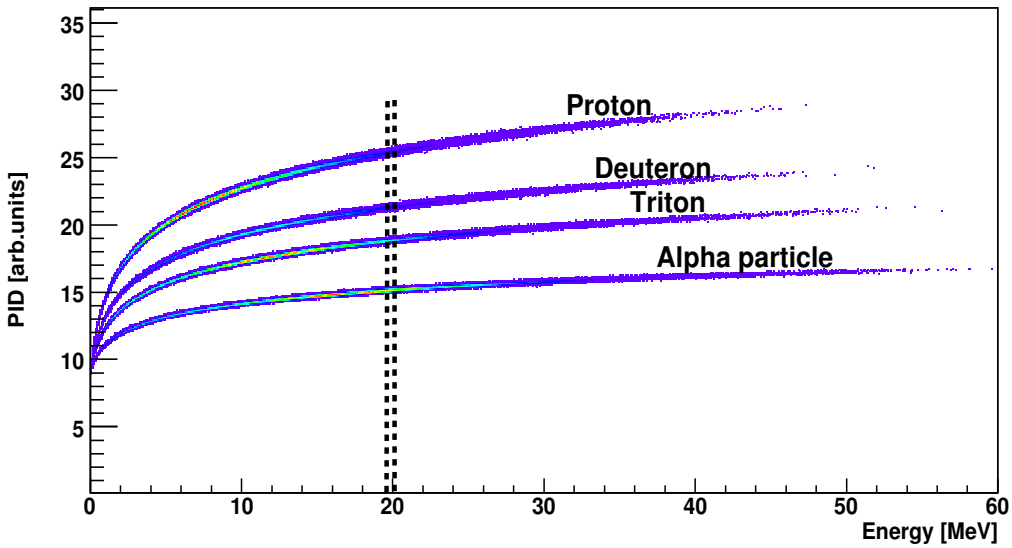

FIG. 5.1. Simulation of the particle identification of the $^{18}O + ^{18}O$ reaction at $E_{lab} = 65$ MeV. The simulation is performed with a light output approximation for particle discrimination.

in the reaction from missing momentum. From the event-by-event file of the CACARIZO code, different particles were identified such as proton, deuteron, triton and α particles. Fig 5.1, illustrates the different particle identification for proton, deuteron and triton and

Particles detected	Reaction Channels Selected
pp	2pxn
p	pxn, α pxn, 2pxn
α	α xn, α pxn
α p	α pxn
α	2α xn
d	dxn, pdxn,
t	txn, ptxn

TABLE. 5.2. Selectivity of all Particle Channels.

α particles since the input file of the simulation contains a combination of these particles.

5.2.2 Simulation of DIAMANT

The main exit channels of the ^{18}O + ^{18}O reaction at E_{lab} = 65 MeV are summarized in Table 5.2 which are the main populated channels of the residual nuclei
For the DIAMANT simulation, the whole geometry of DIAMANT is implemented by defining the area of each square channel detector and its azimuthal and longitudinal angle with respect to the beam axis. These information sets of the geometry of DIAMANT is given as an input file of the SimSort code. Fig. 5.2 is a 3D simulation of the DIAMANT geometry. In this 3D simulation, the number of particles that can be detected in the forward detectors are larger than the backward angles as shown in Fig. 5.2.

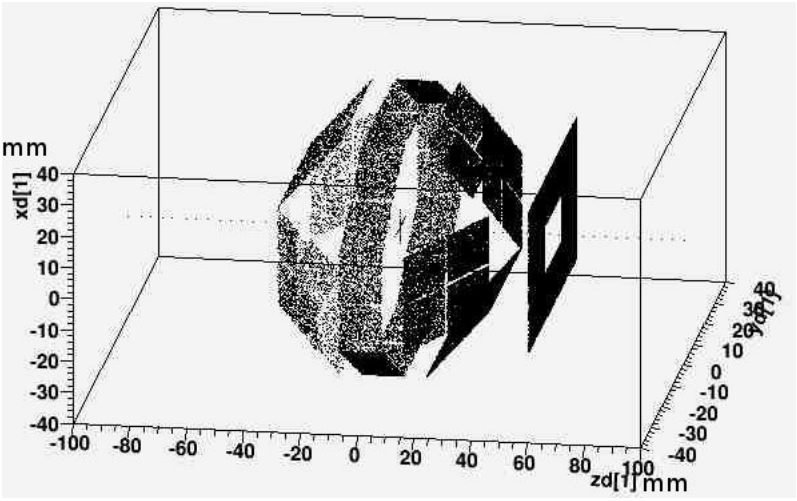

FIG. 5.2. A 3D map simulation of the DIAMANT detector simulated with 10^6 events using SimSort code. The beam comes from left to right, therefore the number of the detected particle in the forward are more than the backward detectors.

Chapter 6

Results and Discussions

This chapter is devoted to the discussion of the results from the experimental data and the comparison to the calculations.

6.1 Deuteron and Triton to Proton Ratio

The first result is the determination of the deuteron to proton ratio (d/p) and the triton to proton ratio (t/p) for some of the residual nuclei identified upon γ-ray transitions. The intensity is determined from the counts integrated in appropriate gates on proton, deuteron and triton and the selection of the ground state transition of the residual nuclei with background subtraction under the total energy γ peak. The ratio is defined by the number of counts of deuteron over the number of counts of proton for d/p ratio and number of counts of triton over the number of counts of proton for t/p ratio. The determination of relative intensities is a way of canceling all unknown parameters relative to the measurements as the integrated charge, dead time, thickness of the target and efficiency of the γ-ray spectrometer. However, the ratio of the different decay channels gated on the particle species does not inform clearly on which of the channel is over- or underestimated. The main transition identified in the $\gamma-\gamma$ matrix have allowed to isolate ^{30}Si and ^{32}P residual nuclei. Regarding ^{32}P, only one charged particle is evaporated from the compound nucleus: *p*, *d* or *t* in *p3n*, *d2n* and *t1n* decay channels respectively. For ^{30}Si, a larger number of channels are open but the main sequences are *2p4n*, *pd3n*, *pt2n*.

Nucleus	γ-ray [keV]	d/p(Exp)	d/p(Simu)
^{32}P	833	0.19 $\pm$ 0.01	0.091
^{32}P	1684	0.23 $\pm$ 0.01	0.091
^{30}Si	1266	0.18 $\pm$ 0.01	0.11

TABLE. 6.1. Experimental and theoretical d/p ratio of ^{32}P and ^{30}Si.

Nucleus	γ-ray [keV]	t/p(Exp)	t/p(Simu)
^{32}P	833	0.06 $\pm$ 0.02	0.09
^{32}P	1684	0.06 $\pm$ 0.02	0.09
^{30}Si	1266	0.08 $\pm$ 0.02	0.04

TABLE. 6.2. Experimental and theoretical t/p ratio of ^{32}P and ^{30}Si.

In Table. 6.1 and 6.2, ^{32}P nucleus is studied from two different transitions because the two transitions, 833 keV and 1684 keV, belong to the same nucleus. The comparison between the experimental and the calculated d/p and t/p ratios are shown in Table. 6.1 and 6.2. The set parameters of the Optical Model (OM) that used for the cascade calculation is under-or-overestimating the cross section of the deuteron and the triton, while the proton cross section is well reproduced. Therefore, the calculated d/p and t/p deviate by a factor of two from the experimental data. These ratios are compared to the d/p and t/p results from Kildir et al [59] for the ^{32}S $+^{64}$Ni reaction at 180 MeV and it shows the same deviation of the calculated cross section from the experimental data using the same set of parameters of the OM. The relative experimental errors are determined in a simple way by the expression 6.1.

$$\sigma = \left(\frac{1}{\sqrt{N_{d,t,\alpha}}} + \frac{1}{\sqrt{N_{bg1}}}\right) + \left(\frac{1}{\sqrt{N_p}} + \frac{1}{\sqrt{N_{bg2}}}\right) \tag{6.1}$$

where $N_{d,t,\alpha}$, N_{bg1} is the number of counts in the d,t and α gated peak and the background associated with these gated peaks respectively. N_p, N_{bg2} is the number of counts in the p gated peak and the background associated with these gated peaks respectively.

6.2 Particle Energy Spectra

Fig. 6.1 and 6.2 show the particle energy spectra of proton and α particles with the comparison between the experimental data and the simulation. The particle energy spectra is the maximum of the energy distribution defined by the Coulomb and the centrifugal barrier is different from proton, deuteron, triton and α particle. The simulations are very important in order to obtain the energy spectra from the center-of-mass frame to the laboratory frame as the energy depends on the emission angle. In addition the CsI detectors have a large opening angle and the simulation takes the response of the detectors. Selection of different residual nucleus of interest is possible through the simulation by requiring the mass number A and the atomic number Z of a certain nucleus. The simulated energy

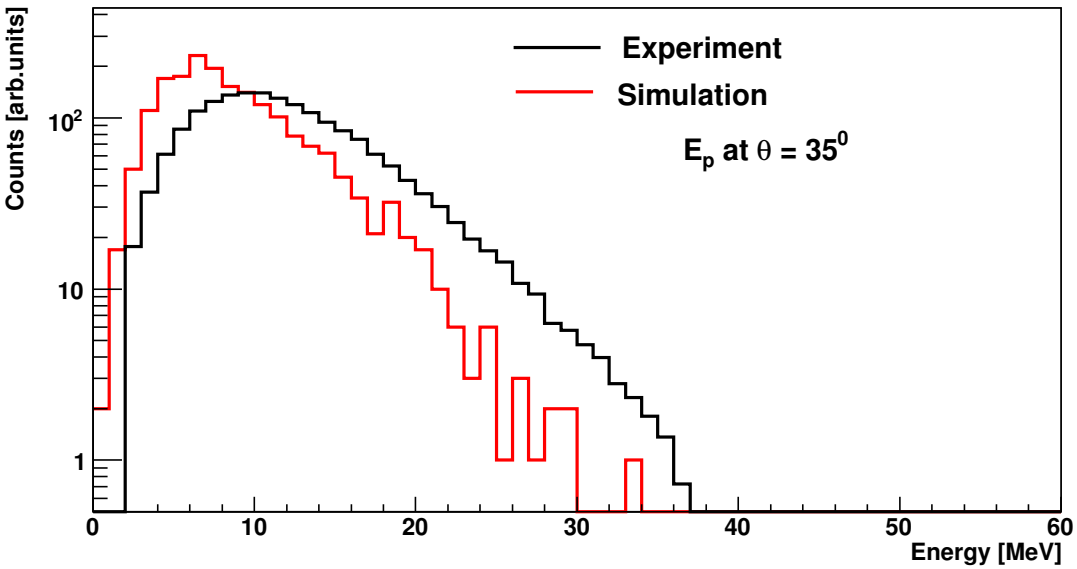

FIG. 6.1. Proton energy spectra from experimental data and simulation of the ^{18}O + ^{18}O reaction at $E_{lab} = 65$ MeV.

spectra have been normalized to the maximum of the experimental ones in order to compare the shapes. Fig. 6.1 shows proton energy spectra from the experimental data which is higher in energy than the simulation which thought to be due to calibration problems with the proton spectra. Noting that the calibration of the proton was performed using the elastic scattering of the ^{1}H(^{16}O,^{1}H) with limited angle to 90°, hence the calibration was done for the detectors in the forward angles only. At 35°, the detectors are calibrated with

proton energy of 7.9 MeV and extrapolated to the all range of energy.

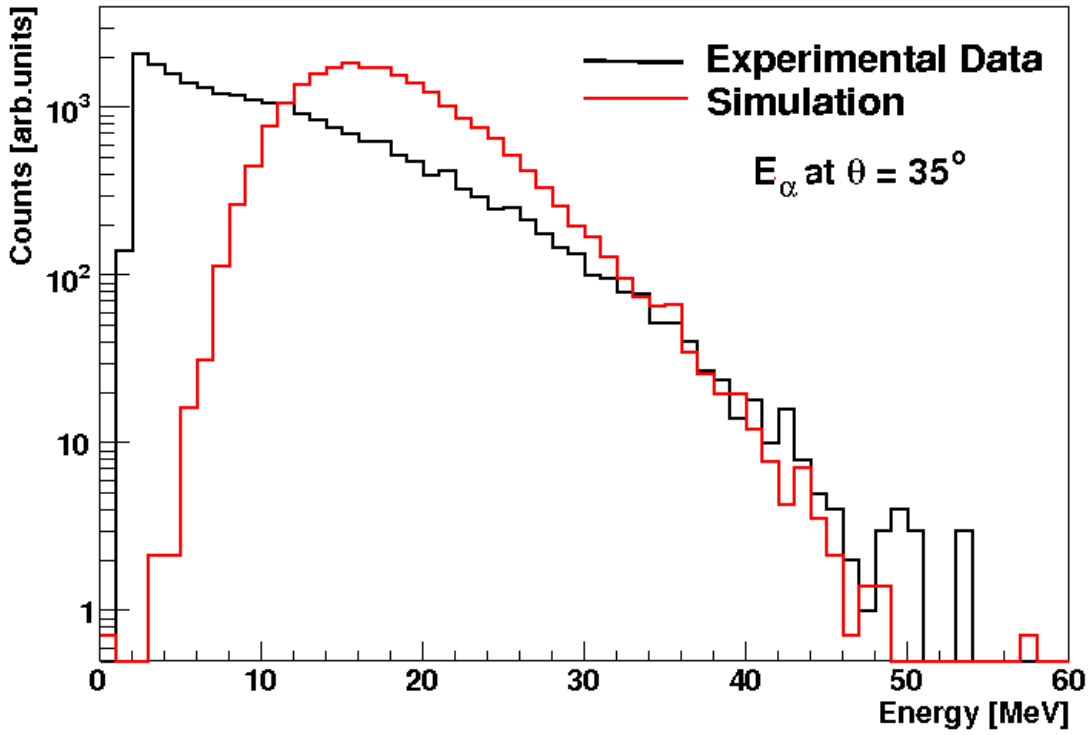

FIG. 6.2. α particle energy spectra from experimental data and simulation of the ^{18}O + ^{18}O reaction at $E_{lab} = 65$ MeV.

The α particle energy spectra illustrated in Fig. 6.2, the low energy part of the experimental spectrum is distorted compared to the simulation. This is due to the absorbers placed in front of the CsI of the DIAMANT detectors during the experiment. In the simulation, the absorbers were not taken into account. The lower energy part of the measured α energy spectrum is distorted as the energy loss is inversely proportional to the incident energy E, the effect is vanishing with increasing energy and the high energy part of the experimental and the simulation spectra coincide. Note also that the energy calibration for α particles was performed with calibration points in the higher energy part of the spectrum. Also, the response of the CsI detectors is not a linear function of the energy deposited by the particle. As a consequence the 0 - 15 MeV energy region is not a true representation of the measured energy E[31]. The deuteron and triton energy spectra are obtained from the experimental data and the simulation as given in Fig. 6.3, 6.4. The non-linear response of

the CsI detector is much less for p, d and t compared to α particles.

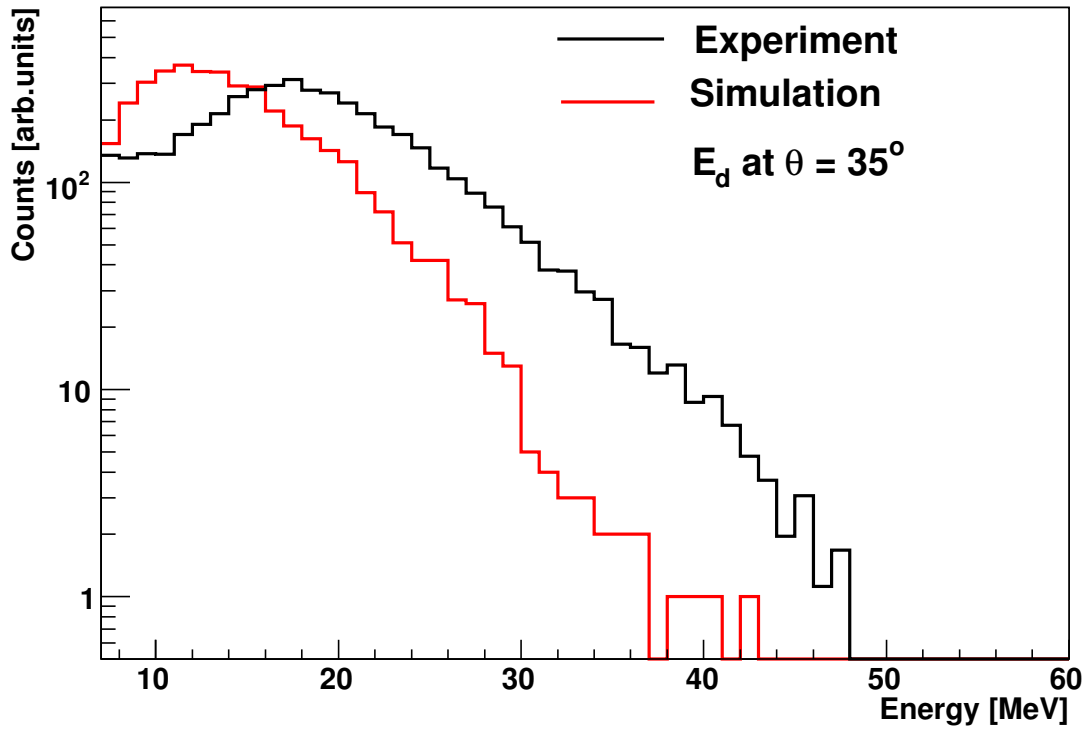

FIG. 6.3. Deuteron energy spectra from the experimental data and the simulation of the ^{18}O + ^{18}O reaction at $E_{lab} = 65$ MeV.

The proton calibration was used to obtain the deuteron and the triton energy spectra as no calibration points were available. However, one can distinguish between the p,d and t spectra. The gradient of the slope at higher energy which depends on the temperature of the emitters in the Maxwellian distribution, is too high. This could indicate a lower temperature of the emitters, but the disagreement with barrier observed for p, d and t comforts the hypothesis of a poor energy calibration.

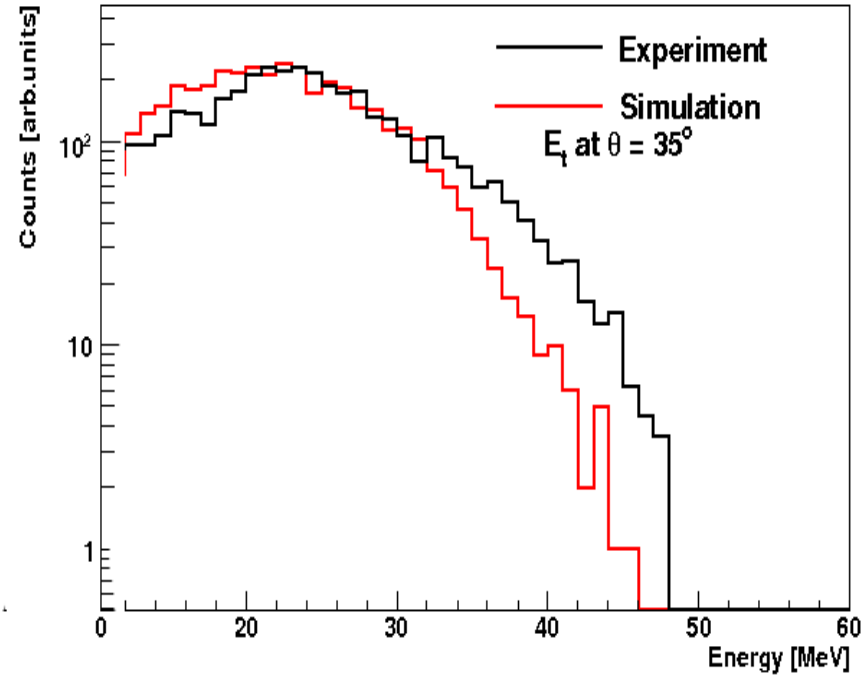

FIG. 6.4. Triton energy spectra from experimental data and simulation of the ^{18}O + ^{18}O reaction at $E_{lab} = 65$ MeV obtained at $E_t = 35$.

Chapter 7

Conclusions

In this thesis, fusion evaporation channels were studied in the ^{18}O + ^{18}O reaction at E_{lab} = 65 MeV. The experiment was performed at iThemba LABS using the SSC accelerator facility to produce the ^{18}O beam and the AFRODITE γ-ray spectrometer with the DIAMANT detector for charged particles. A solid oxygen target was obtained from the oxidation of natural Ta material. The AFRODITE and DIAMANT were set in coincidence to trigger between light charged particles and γ-rays. The data analysis was carried out using the SimSort computer program within the ROOT package. Sulphur-36 was populated as a compound nucleus in the ^{18}O + ^{18}O reaction with excitation energy E_x = 61.6 MeV. The population of selected evaporation residue was investigated through various evaporation channels. Protons, deuterons, tritons and α particles were identified together with known γ-ray lines of evaporation residues. The computer code CACARIZO, the Monte Carlo version of CASCADE, was used to calculate the relative cross-section of the residual nuclei populated in the ^{18}O + ^{18}O reaction at E_{lab} = 65 MeV. Emission of light charged particles, p, d, t and α are observed. The measured d/p and t/p ratios for very selective transitions of the evaporation channels were compared to the CASCADE calculations and found to be in good agreement. The energy spectra of proton, deuteron, triton and α particles were simulated and compared to the experimental data using the CASCADE calculations and the SimSort code to convert the center-of-mass data in the laboratory frame. Discrepancies arise mostly due to the lack of calibration points and the energy loss of particle through absorbers which was neglected in a first approximation. This work is the first attempt of an energy calibration of the DIAMANT detector at iThemba LABS. Implementation of

absorbers in the simulations should greatly improve the determination of energy distribution of charged particles. Further work requiring good energy calibration should include dedicated calibration runs. This is not an obvious task as changing the beam species and energy is a time consuming task with the SSC accelerator. However, the use of 66 MeV proton, often available at iThemba LABS facility, impinging on various targets such as deuteron enriched plastic to heavy elements such as Au would provide a number of useful calibration points.

Bibliography

[1] A. V. Ignatyuk. Fusion evaporation. http://nrv.jinr.ru/nrv/, 2010.

[2] A. V. Ignatyuk et al. Decay of excited nuclei. *Sov. J. Nucl. Phys*, **21**:612, 1975.

[3] B. M. Nyakò et al. Performance of the diamant detector at ganil and plans for improvements. ATOMKI laboratory: for the DIAMANT collaboration, (unpublished).

[4] G. F. Knoll. *Radiation Detection and Measurement*. John Willey & Sons, New York Chichester Brisbane Toronto, 1979.

[5] H. J. Wollersheim. Peak-to-total ratio. http://www-linux.gsi.de/wolle/GSICLOVER/clover/node8.html, 2000.

[6] B. M. Msezane. The study of high-spin states in ^{196}Hg. Master's thesis, University of Zululand, 2006 MSc Thesis.

[7] G. Viesti et al. Decay of deformed ^{59}Cu nuclei. *Phys.Rev. C*, **38**:2640–2657, 1988.

[8] A. Gavron. Pace. *Phys. Rev*, **C21**:230, 1980.

[9] Charity et al. Gemini. *Nucl. Phys*, **A483**:371, 1988.

[10] Pühlhofer. Cascade. *Nucl. Phys*, **A280**:267, 1977.

[11] A. Bohr and B. R. Mottelson. *Nuclear Structure*. World Scientific Publishing, 1969 and reissue 1998.

[12] D. Mahboub et al. Light particle emission in ^{35}Cl + ^{24}Mg fusion reactions at high excitation energy and angular momentum. *Phys. Rev. C*, **69**(3):034616, March 2004.

[13] P. E Hodgson. Compound nucleus reactions. *Rep. Prog. Phys*, **50**:1171–1228, 1987.

[14] T. Matsuse et al. Extended hauser-feshbach method for statistical binary-decay of light-mass system. *Phys. Rev. C*, **55**:1380–1393, 1997.

[15] K. S. Krane. *Introductory Nuclear Physics*. John Wiley & Sons, Canada, 1988.

[16] P. E. Hodgson. *Nuclear heavy-ion reactions*. Oxford university press, 1978.

[17] W. Greiner, T. Y. Park, and W. Scheid. *Nuclear molecules*. World Scientific publishing, 1995.

[18] H. V. Buttlar. *Nuclear physics an introduction*. Academic Press, INC,111 5^{th} Avenue, New York, New York 10003, 1964.

[19] C. A. Engelbrecht and H. A. Weidenm üller. Hauser-Feshbach Theory and Ericson Fluctuations in the Presence of Direct Reactions. *Phys. Rev. C*, **8**:859–862, 1973.

[20] M. Blann et al. Calculation of γ-ray cascades in the code ALICE. *Nucl. Inst. and Meth. in Phys. Res. A*, **265**:490–494, 1988.

[21] Kulko et al. Isomeric ratios for ^{196,198}Tl and ^{196,198}Au from fusion and transfer in the interaction of ^{6}He with ^{197}Au. *J. Phys. G: Nucl. Part. Phys.*, **34**:2297–2306, 2007.

[22] A. Gavron. *Phys. Rev. C*, **21**:230, 1980.

[23] J. Gomez del Campo et al. Comparison of fusion cross sections for the ^{10}B + ^{16}O and ^{12}C + ^{14}N systems. *Phys. Rev. C*, **29**:1722 – 1734, 1984.

[24] D. V. Vanin et al. Langevin calculations of fission fragment mass distribution in fission of excited nuclei. *Phys. Rev.C*, **59**:2114–2121, April 1999.

[25] F. Pühlhofer et al. Isotop and element distribution of the evaporation residues from fusion of 160 MeV ^{32}S with ^{24,25,26}Mg and ^{27}Al. *Phys. Rev.C*, **16**:1010–1019, Sept 1977.

[26] B. Fornal et al. Level density of hot nuclei with A $\leq$ 40. *Phys. Rev.C*, **44**:2588–2597, December 1991.

[27] P. Fröbrich and R. Lipperheide. *Theory of nuclear reactions*. Oxford University Press, 1996.

[28] E. A. M. A. Khaleel. *Superheavy Elements: Search and Discovery.* AIMS Essay, 2008.

[29] M. Brekiesz et al. Study of deformation effects in the charged particle emission from ^{46}Ti. *Act. Phys. Polo. B*, **36**(4), 2005.

[30] J. Wilczynski. Calculations of the critical angular momentum in the entrance reaction channel. *Nucl. Phys. A*, **216**:386–394, 1973.

[31] P. Papka. *Etude de la désexcitstion par particules légères chargées du noyau ^{44}Ti.* PhD thesis, Louis Pasteur University, 2003.

[32] A. Das and T. Ferbel. *Introduction to Nuclear and Particle Physics.* World Scientific Publishing Co. Pte. ltd, 57 Shelton Street, Convent Garden, London WC2H 9HE., 2003.

[33] G. K. Mabala. *Dipole Bands in ^{195}Bi and ^{197}Bi nuclei.* PhD thesis, 2003.

[34] P. Castellaz et al. Chemical reaction of positronium studied by age-momentum correlation (anoc) using a relativistic positron beam. *Radio. Nucl. Chemist*, **201**:457–467, 1996.

[35] T. Goworek. Positronium as a probe of small free volume. *Nucl. Radio. Scie.*, **1**:11–13, 2000.

[36] S. G. Karshenboim. Precision Study of Positronium: Testing Bound State QED Theory. *Int. J. Mod. Phys. A*, **19**:3879–3896, 2004.

[37] P. A. Vetter and S. J. Freedman. Branching-ratio measurements of multiphoton decays of positronium. *Phys. Rev. A*, **66**:052505, 2002.

[38] G. Nelson and D. Reilly. Gamma-ray interactions with matter. www.fas.org/sgp/othergov/doe/lanl/lib-www/la.../00326397.pdf.

[39] R. F. Casten. *Nuclear structure from a simple perspective.* Oxford University Press, Biddles Hd, Guildford and Kings Lynn, 2000.

[40] M. Lipoglavsek et al. Measuring high-energy γ-rays with Ge clover detectors. *Nucl. Inst. and Meth. in Phys. Res. Sect. A*, **557**:523–527, 2006.

[41] L. Jian-Ling et al. Characteristics of a 4-fold segmented clover detectors. *Chin. Phys. C*, **33**:202, 2009.

[42] M. S. Sarkara et al. Characterisation of a Compton suppressed Clover detector for high energy gamma rays ($\leq$ 11 MeV). *Nuclear Instruments and Methods in Physics research A*, **556**:266–272, 2006.

[43] T. E. Madiba. Directional correlation from oriented states and linear polarization measurements of gamma rays from ^{190}Ti. Master's thesis, University of the Westren Cape, 2008 MSc Thesis.

[44] F. A. Beck et al. The clover detector. *IAEA NCLCollectionStore*, **CA9700507**:364–368.

[45] S. P. Bvumbi. Spin and parity assignment in ^{152}Gd investigation octupole structures. Master's thesis, University of the Western Cape, 2008 MSc Thesis.

[46] J. Gál et al. The VXI electronics of the DIAMANT particle detector array. *Nucl. Inst. & Meth. in Phys. Res. A*, **516**:502–510, August 2004.

[47] K. Andgren. *Studies of collective phenomena in neutron deficient nuclei*. PhD thesis, 2008.

[48] R. Laforest et al. Particle identification with faust detector. *Nucl. Inst. and Meth. in Phys. Res. Sect. A*, **40**:470–472, February 1998.

[49] M. Alderighi et al. Particle identification method in the CsI(Tl) scintillator used for the chimera 4π detector. *Nucl. Inst. and Meth. in Phys. Res. A*, **489**:257–265, 2002.

[50] T. D. Singo. Search for non-yrast states in ^{160}Yb. Master's thesis, University of Cape Town, 2008 MSc Thesis.

[51] S. Ritt. Midas. https://midas.psi.ch/, Feb 2001.

[52] J. A. Swartz. A Feasibility Study of the (^{3}He, ^{8}He) Reaction with the K600 Magnetic Spectrometer. Master's thesis, University of Stellenbosch, 2010 MSc Thesis.

[53] R. Brun, F. Rademakers, and the ROOT team. Root. http://root.cern.ch/, December 2008.

[54] P. Papka et al. Decay path measurements for the 2.429 MeV state in ^{9}Be: Implications for the astrophysical $\alpha + \alpha +$ n reaction. *Phys. Rev. C*, **75**:045803, 2007.

[55] P. Papka et al. Decay of ^{6}Be populated in the ^{6}Li(^{3}He,^{3}H) charge-exchange reaction. *Phys. Rev. C*, **81**:054308, 2010.

[56] P. Wagner et al. Electromagnetic properties of low-lying ^{26}Mg states. *Phys. Rev. C*, **11**:1622–1633, 1975.

[57] D. Radford. Radware coincidence finder. http://radware.phy.ornl.gov/cf.html, May 1999.

[58] P. Papka. General analysis and simulation code for nuclear physics.

[59] M. Kildir et al. ^{1,2,3}H, ^{4} He emission from ^{96}Ru nuclei (E* = 113 MeV): Test for transmission coefficients in the evaporation model. *Phys.Rev. C*, **46**:2246–2272, 1992.

[60] S. Ota. Fusion evaporation reaction. http://www.cns.s.u-tokyo.ac.jp/nuspeq/index.php?Glossary%2FFusionReaction, Jun 2009.

[61] N. Bohar and J. A. Wheeler. The mechanism of nuclear fission. *Phys. Rev*, **56**:426–450, Sept 1939.